



# Analysis of rotorcraft ground resonance with generic inter-blade damper configurations

Vincenzo Muscarello<sup>1</sup> · Giuseppe Quaranta<sup>2</sup>

Received: 13 June 2022 / Revised: 28 November 2022 / Accepted: 11 January 2023 / Published online: 7 February 2023  
© The Author(s) 2023, corrected publication 2023

## Abstract

The paper investigates the effect of inter-blade dampers with generic in-plane and out-of-plane attachment offsets on ground resonance stability proneness. An analytical formulation, considering dampers with radial offsets only is initially proposed. Sensitivity analyses show that the increase of radial offset reduces the cyclic lead-lag damping and stiffness, providing a non-zero contribution to collective terms. The analytical formulation is suitable, in a preliminary design phase, to define the optimal location of the inter-blade attachment points to avoid ground resonance phenomena and to stabilize the engine drive-train dynamics. A more detailed numerical approach is then presented to consider generic in-plane and out-of-plane attachment offsets. Ground resonance stability analyses are performed also for cases with dissimilar dampers. It is found that out-of-plane offset leads to a modification on the blade pitch-lag coupling, acting on the helicopter stability margins. However, to capture these effects it is necessary to include the overall blade motions, considering flap, lag, and pitch dynamics, together with the corresponding generalized aerodynamics forces, usually neglected in classical ground resonance analysis. Finally, the periodic stability with one damper inoperative shows how, with the radial offsets, the hybridized lead-lag collective and cyclic modes may fall into resonance conditions due to super-harmonics.

**Keywords** Helicopter ground resonance · Inter-blade dampers · Periodic stability · Anisotropic rotors

## List of symbols

$\mathbb{A}$	Periodic state matrix
$\mathbf{A}_H, \mathbf{B}_H, \mathbf{C}_H$	Helicopter state-space matrices
$a$	Distance between damper inboard offset and lead-lag hinge offset
$b$	Distance between damper outboard offset and lead-lag hinge offset
$c$	Distance between lead-lag hinges
$\mathbb{C}, \mathbb{K}$	Generalized inter-blade damping and stiffness matrices

$\mathbb{C}, \mathbb{K}$	Inter-blade damping and stiffness matrices
$C_\zeta$	Lead-lag viscous damping
$c_d, k_d$	Damper viscous and elastic coefficients (equal dampers)
$c_i, k_i$	$i$ th Damper viscous and elastic coefficients
$E_{f_c}$	Damping effectiveness ratio
$E_{f_k}$	Stiffness effectiveness ratio
$e_\zeta$	Lead-lag hinge offset
$F_i$	$i$ th Damper restoring force
$h = (a + b)/2$	Damper radial average position
$i$	Imaginary unit
$K_\zeta$	Lead-lag spring stiffness
$K_{p_\zeta}$	Pitch-lag coupling, positive for lag back, pitch down
$\ell_i$	$i$ th Damper length
$\ell_0$	Damper undeformed length
$N_b$	Number of blades
$o = b - a$	Damper radial offset
$Q_i$	Inter-blade restoring torque on the $i$ th blade
$R$	Rotor radius
$\mathbf{T}$	Multiblade transformation matrix
$T = \frac{2\pi}{\Omega}$	Rotor time period

Vincenzo Muscarello and Giuseppe Quaranta have contributed equally to this work.

✉ Vincenzo Muscarello  
vincenzo.muscarello@rmit.edu.au  
Giuseppe Quaranta  
giuseppe.quaranta@polimi.it

<sup>1</sup> School of Engineering, Aerospace Engineering and Aviation, RMIT University, 264 Plenty Rd, Melbourne, VIC 3082, Australia

<sup>2</sup> Department of Aerospace Science and Technology, Politecnico di Milano, Via La Masa 34, Milan 20156, Italy

$t$	Time
$W$	Work
$\gamma_i$	$i$ th Damper orientation
$\Delta$	Perturbation about equilibrium condition
$\Delta\psi$	Azimuthal offset between two adjoining blades
$\delta$	Virtual quantity
$\zeta_i$	Lead-lag rotation referred to the $i$ th blade (positive lag)
$\eta_j$	$j$ th Floquet characteristic exponent
$\theta$	Blade pitch angle
$\Lambda_j$	$j$ th Floquet characteristic multiplier
$\xi_k$	Damping ratio of the $k$ th-mode
$\sigma$	Eigenvalue, real part
$\phi = \frac{\pi - \Delta\psi}{2}$	Rotor geometric angle
$\psi$	Azimuth angle
$\psi_i$	Azimuth position of the $i$ th blade
$\Omega$	Rotor speed
$\omega$	Eigenvalue, imaginary part
$\omega_k$	Natural frequency of the $k$ th-mode
$\times$	Cross product
$(\dot{\cdot}) = \frac{d}{dt}$	Time derivative
$(\cdot) _E$	Variable evaluated at the equilibrium condition
$(\cdot)^R$	Variable evaluated in the rotating reference frame
$(\cdot)^{NR}$	Variable evaluated in the non-rotating reference frame
$0, n_c, n_s, S$	Degrees of freedom of the Multiblade Coordinate Transformation
$\Re$	Real part
$\Im$	Imaginary part

## 1 Introduction

Rotorcraft with articulated soft in-plane rotors require the use of lead-lag dampers to avoid ground resonance (GR) stability problems. This phenomenon is designed as a dynamic instability that involves the coupling of the cyclic lead-lag motion of the main rotor blades with the helicopter body motion. GR was first addressed in 1943 by Coleman [1], and subsequently investigated by Deutsch [2] in 1946. However, the main reference work on GR remains the technical report released by Coleman and Feingold in 1958 [3]. Generally, the instability is characterized by a resonance of the regressive cyclic lead-lag mode of the main rotor and a natural frequency of the structure supporting the rotor. A resonance is possible when the rotating lead-lag frequency  $\nu_\zeta$  is below 1/rev, as for articulated

and soft in-plane hingeless rotors. With articulated rotors, the critical mode is usually an oscillation of the helicopter on the landing gear when in contact with the ground, hence the name Ground Resonance. The phenomenon may occur in flight as well, due to the coupling of the lead-lag cyclic modes with the low-frequency airframe modes related to flight dynamics; in this case, it is called Air Resonance [4, 5]. GR is potentially destructive; avoiding this instability is fundamental in helicopter design. Generally, resonances ranging from 40% to 120% of the nominal rotor speed are not acceptable. Within this range, therefore, it is necessary to either avoid resonances or provide sufficient damping in the system to prevent any instability.

In the last few years, several studies have been performed to prove the benefits of inter-blade dampers in increasing GR stability margins. The key element of the inter-blade configuration is the ability to work mainly for relative lead-lag degrees of freedom, due to the connection between each blade and the previous/following one. Sela and Rosen [6] were the first who investigated the GR with inter-connected blade dampers. The results of their work clearly showed the advantages of this configuration on GR stability concerning the classical “blade-to-hub” damper connection, when considering rotors with less than six blades. As a matter of fact, the inter-connecting dampers were shown to be more effective than the corresponding dampers with the classical blade-to-hub configuration for most rotors. A few years later, an extension of this work was proposed by the same authors, by changing the arrangement of the inter-blade connections to have a more effective solution for rotors with more than five blades [7]. Sela and Rosen [8] also investigated the influence of inter-blade connections and variable rotor speed on the aeromechanical stability of a helicopter, showing that the hub rotational degree of freedom can interact with the regressing lead-lag degree of freedom and alter the stability of the system. Masarati et al. investigated more complex inter-2-blade configurations [9] that, however, have not been applied up to now to any flying aircraft.

Indeed, the baseline inter-blade damper model proposed by Sela and Rosen requires that, on a specific blade, the attachment points of the front and rear damper are identical. This configuration increases the damping of the lead-lag cyclic (and scissor) modes compared to the classical blade-to-hub configuration, thus improving GR stability boundaries. On the other side, the lead-lag collective mode remains poorly damped since its only source of damping, due to the in-plane aerodynamic loads, is usually small. This blade motion is generally coupled with the torsional dynamics of the engine drive train system of the helicopter, which can potentially be unstable for high gains in the fuel control system [10].

To overcome this problem a radial, spanwise, offset can be considered on inter-blade damper attachment points, to

provide an amount of damping also on the lead-lag collective dynamics.

Additionally, as remarked by Kryszynski et al. in Ref. [10], the blade feathering motion can play an important role in inter-blade damper kinematics. So, in general, in-plane and out-of-plane displacements of damper attachment points should be considered.

Rotor blades with inter-connected visco-elastic dampers were also investigated by Suresh and Nagabhushanam for an isolated rotor [11], and a rotor-body system [12]. A rigid flap-lag rotor model was used in the analysis, neglecting the blade feathering motion and considering equal spanwise damper attachment points without offsets. The results demonstrated that rotor loads, dynamic response, and stability heavily depend on the inter-blade visco-elastic parameters.

Brackbill et al. [13] addressed the influence of attachment offsets on aeromechanical stability and response of helicopters with nonlinear inter-blade elastomeric dampers, including the blade feathering motion in the damper kinematic relations. The main results demonstrated that one particular combination of offsets was able to reduce the damper 1/rev displacement by 60% compared to the baseline configuration, reducing damper fatigue.

The present paper aims to investigate the effect of inter-blade dampers with different in-plane and out-of-plane attachment offsets on GR stability, exploiting a detailed helicopter aeroelastic model. As far as the authors' knowledge, a comprehensive study has not yet been presented in the open literature. Initially, an analytical inter-blade damper model with only radial attachment offsets is proposed and sensitivity analyses to the main geometrical parameters are performed to highlight the difference between (1) the baseline inter-blade configuration without offsets and (2) the classical blade-to-hub configuration (Sect. 2). Subsequently, a more detailed layout is presented considering in-plane and out-of-plane attachment offsets for the inter-blade damper (Sect. 3). The helicopter model used in this work is representative of the IAR330 Puma, a medium-size rotorcraft with four blades, manufactured by IAR Braşov. GR stability analyses with generic inter-blade dampers are then performed, evaluating the pros and cons of each configuration in Sect. 4. Periodic stability analyses are finally conducted through the Floquet theory for the cases where one damper results inoperative. Section 5 ends by drawing some conclusions.

## 2 An analytical inter-blade damper model with radial attachment offsets

In this section, a simple inter-blade damper model with only radial offsets is proposed. The corresponding damping and stiffness matrices are computed analytically and the sensitivity analysis to the main geometrical parameters is performed.

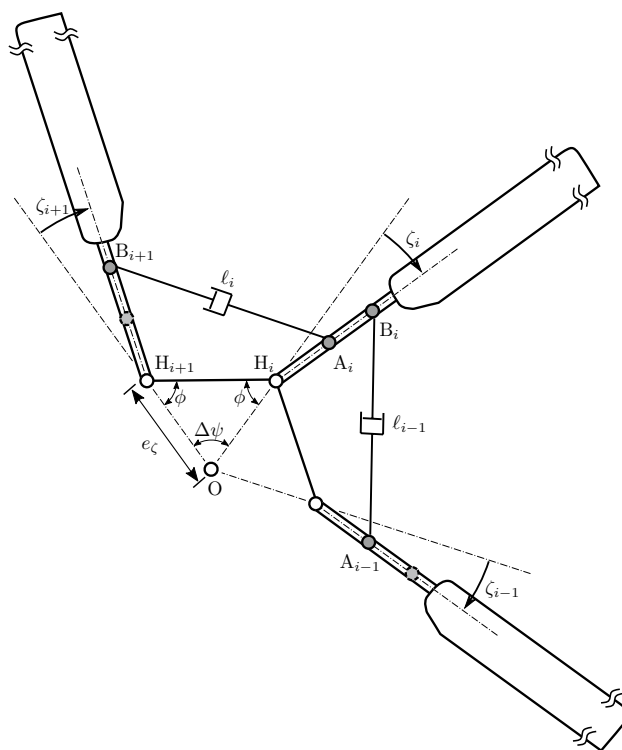


Fig. 1 Top view of the rotor model with inter-connected blades

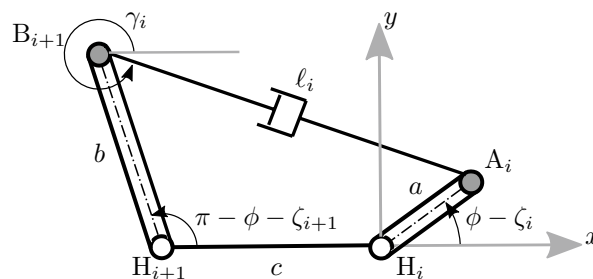


Fig. 2 Kinematic model for inter-connected blades

Figure 1 depicts the rotor with inter-connected blades. The model lies in the rotor plane. The hub is placed in the rotor center O, and the lead-lag hinges are characterized by a radial offset  $e_c$ . The subscript  $i$  is referred to the generic  $i$ th blade while the inter-blade attachment points are located in the radial stations A (inboard) and B (outboard) on each blade. Let's call the distance between the inboard offset and the lead-lag hinge  $\|(\mathbf{r}_{A_i} - \mathbf{r}_{H_i})\| = a$ . Similarly, the distance between the outboard offset and the lead-lag hinge is  $\|(\mathbf{r}_{B_i} - \mathbf{r}_{H_i})\| = b$ . For a generic rotor with  $N_b$  blades, the azimuthal offset is equal to  $\Delta\psi = \frac{2\pi}{N_b}$ . The  $\phi$  angle is  $\frac{\pi - \Delta\psi}{2}$  while the distance between the lead-lag hinges is  $c = 2e_c \sin \frac{\Delta\psi}{2}$ . In this model, only the lead-lag

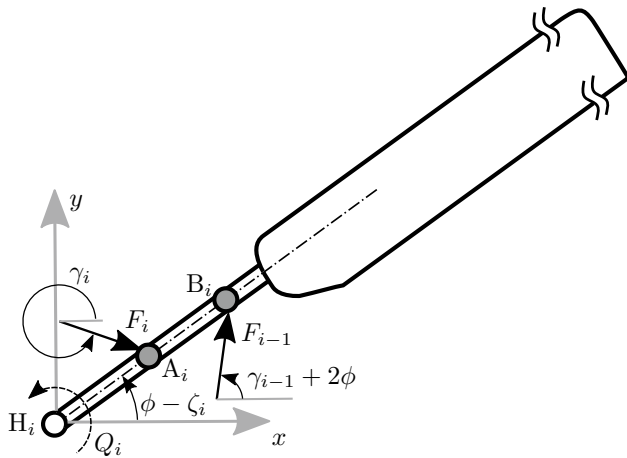


Fig. 3 Restoring torque on generic  $i$ -th blade

degrees of freedom,  $\zeta_i$ , with  $i = 1, \dots, N_b$ , are taken into account.

The kinematic model is shown in Fig. 2. The next steps will help the reader to determine the damper length  $\ell_i$  and orientation  $\gamma_i$  as a function of the lead-lag rotations  $\zeta_i$  and  $\zeta_{i+1}$  related to the connected blades.

The kinematic relationship can be easily obtained by considering the quadrilateral with vertexes  $H_i$ ,  $A_i$ ,  $B_{i+1}$ , and  $H_{i+1}$ . The vector loop equation returns two scalar equations:

$$\ell_i \cos \gamma_i + b \cos (\pi - \phi - \zeta_{i+1}) = a \cos (\phi - \zeta_i) + c, \quad (1a)$$

$$\ell_i \sin \gamma_i + b \sin (\pi - \phi - \zeta_{i+1}) = a \sin (\phi - \zeta_i), \quad (1b)$$

whose solution yields

$$\ell_i^2 = [c + a \cos (\zeta_i - \phi) + b \cos (\zeta_{i+1} + \phi)]^2 + [a \sin (\zeta_i - \phi) + b \sin (\zeta_{i+1} + \phi)]^2, \quad (2)$$

and

$$\tan \gamma_i = -\frac{a \sin (\zeta_i - \phi) + b \sin (\zeta_{i+1} + \phi)}{c + a \cos (\zeta_i - \phi) + b \cos (\zeta_{i+1} + \phi)}. \quad (3)$$

Velocity relationships can be easily obtained through the time derivatives of Eq. 1, namely:

$$\dot{\ell}_i = -a \sin (\zeta_i - \phi + \gamma_i) \dot{\zeta}_i - b \sin (\zeta_{i+1} + \phi + \gamma_i) \dot{\zeta}_{i+1}, \quad (4a)$$

$$\dot{\gamma}_i = -\frac{a}{\ell_i} \cos (\zeta_i - \phi + \gamma_i) \dot{\zeta}_i - \frac{b}{\ell_i} \cos (\zeta_{i+1} + \phi + \gamma_i) \dot{\zeta}_{i+1}, \quad (4b)$$

The torque  $Q_i$  on the generic  $i$ th blade due to the interconnected dampers can be evaluated through the moment of the two damper forces acting on the two attachment points  $A_i$  and  $B_i$ , shown in Fig. 3, as:

$$Q_i = aF_i \sin (\zeta_i - \phi + \gamma_i) + bF_{i-1} \sin (\zeta_i + \phi + \gamma_{i-1}), \quad (5)$$

where the force  $F_i$  can be represented either by a linear or nonlinear constitutive law, depending on the damper elongation  $\ell_i$  and on its time derivative  $\dot{\ell}_i$ .

For ground resonance stability analyses, the torque must be firstly linearized about an equilibrium condition and then reported in the non-rotating reference frame using the Multi-blade Coordinate Transformation (MCT), to restore a set of Linear Time Invariant (LTI) equations [1]. Considering the lead-lag degrees of freedom, and the kinematic relationships previously obtained, the torque applied to the  $i$ th blade is influenced by the lead-lag rotations and angular velocities of the two adjoining blades, in addition to the own blade contribution. The linearization of the  $i$ th torque yields:

$$Q_i \approx Q_i \Big|_E + \frac{\partial Q_i}{\partial \zeta_{i-1}} \Big|_E \Delta \zeta_{i-1} + \frac{\partial Q_i}{\partial \zeta_i} \Big|_E \Delta \zeta_i + \frac{\partial Q_i}{\partial \zeta_{i+1}} \Big|_E \Delta \zeta_{i+1} + \frac{\partial Q_i}{\partial \dot{\zeta}_{i-1}} \Big|_E \Delta \dot{\zeta}_{i-1} + \frac{\partial Q_i}{\partial \dot{\zeta}_i} \Big|_E \Delta \dot{\zeta}_i + \frac{\partial Q_i}{\partial \dot{\zeta}_{i+1}} \Big|_E \Delta \dot{\zeta}_{i+1}. \quad (6)$$

The six derivatives can be computed using the kinematic and dynamic relationships previously obtained. The subscript  $|_E$  is added to remind the evaluation of the derivatives at the equilibrium condition. Of course, the lead-lag damper constitutive law must be established. In this context a simple linear constitutive law is proposed, namely:

$$F_i = -c_i \dot{\ell}_i - k_i (\ell_i - \ell_0), \quad (7)$$

where  $c_i$  and  $k_i$  are, respectively, the viscous and elastic coefficients of the  $i$ th damper and  $\ell_0$  its undeformed length. It should be remembered that for stability analyses the non-linear constitutive law, due to a hydraulic or elastomeric damper, is typically approximated by a quasi-linear model, where a dependence is left on the amplitude and frequency of the input excitation [14, 15].

The derivatives in Eq. 6, evaluated at the equilibrium condition, are reported in the following considering equal dampers with  $c_d = c_1, \dots, c_{N_b}$  and  $k_d = k_1, \dots, k_{N_b}$ , namely

$$K_{\zeta_d} = \frac{\partial Q_i}{\partial \zeta_i} \Big|_E = a^2 k_d \sin^2 (\zeta_E - \phi + \gamma_E) + b^2 k_d \sin^2 (\zeta_E + \phi + \gamma_E) + a k_d \frac{(\ell_E - \ell_0)}{\ell_E} \cos (\zeta_E - \phi + \gamma_E) [\ell_E - a \cos (\zeta_E - \phi + \gamma_E)] + b k_d \frac{(\ell_E - \ell_0)}{\ell_E} \cos (\zeta_E + \phi + \gamma_E) [\ell_E - b \cos (\zeta_E + \phi + \gamma_E)], \quad (8a)$$

$$C_{\zeta_d} = \left. \frac{\partial Q_i}{\partial \dot{\zeta}_i} \right|_E = a^2 c_d \sin^2 (\zeta_E - \phi + \gamma_E) + b^2 c_d \sin^2 (\zeta_E + \phi + \gamma_E), \tag{8b}$$

$$K_{\zeta_{ed}} = \left. \frac{\partial Q_i}{\partial \zeta_{i-1}} \right|_E = \left. \frac{\partial Q_i}{\partial \zeta_{i+1}} \right|_E = abk_d \sin (\zeta_E - \phi + \gamma_E) \sin (\zeta_E + \phi + \gamma_E) + abk_d \frac{(\ell_E - \ell_0)}{\ell_E} \cos (\zeta_E - \phi + \gamma_E) \cos (\zeta_E + \phi + \gamma_E), \tag{8c}$$

$$C_{\zeta_{ed}} = \left. \frac{\partial Q_i}{\partial \dot{\zeta}_{i-1}} \right|_E = \left. \frac{\partial Q_i}{\partial \dot{\zeta}_{i+1}} \right|_E = abc_d \sin (\zeta_E - \phi + \gamma_E) \sin (\zeta_E + \phi + \gamma_E), \tag{8d}$$

where  $\zeta_E$  is the equilibrium lead-lag angle, corresponding to the lead-lag mean component in trim condition, while  $\ell_E$  and  $\gamma_E$  can be computed using Eqs. 2, 3. Note that, if  $\ell_E \neq \ell_0$ , a prestress contribution is added to the stiffness terms. Thus, rewriting all perturbation torques as a function of the lead-lag rotations and angular velocities the following compact equation, in matrix form, can be obtained:

$$\Delta \mathbf{Q}^R = \mathbf{C}^R \cdot \Delta \dot{\boldsymbol{\zeta}}^R + \mathbf{K}^R \cdot \Delta \boldsymbol{\zeta}^R, \tag{9}$$

where  $\Delta \mathbf{Q}^R = \{\Delta Q_1, \dots, \Delta Q_{N_b}\}^T$  collects the torques on each blade and  $\Delta \boldsymbol{\zeta}^R = \{\Delta \zeta_1, \dots, \Delta \zeta_{N_b}\}^T$  the lead-lag degrees of freedom involved. Please, note that the superscript ‘‘R’’ is introduced to remind the reader that all the equations are written in a rotating reference frame with constant rotational speed  $\Omega$ . For analyzing aeromechanical stability problems the equations of motion are generally written in a non-rotating reference frame. For isotropic rotors, the equations are transformed into constant coefficient equations and the rotor is viewed as a whole. The single-blade degree of freedom can be obtained from the multiblade coordinates as

$$q_i = q_0 + \sum_{n=1}^{N_b^*} (q_{nc} \cos n\psi_i + q_{ns} \sin n\psi_i) + q_S (-1)^i \tag{10}$$

where  $N_b^* = (N_b - 1)/2$  if  $N_b$  is odd, or  $N_b^* = N_b/2 - 1$  if  $N_b$  is even. The transformation between the rotating and non-rotating degrees of freedom, in matrix form, yields:

$$\begin{pmatrix} q_1 \\ \vdots \\ q_i \\ \vdots \\ q_{N_b} \end{pmatrix} = \begin{pmatrix} 1 & \cos \psi_1 & \sin \psi_1 & \cos 2\psi_1 & \sin 2\psi_1 & \dots & -1 \\ \vdots & \vdots & \vdots & \vdots & \vdots & \vdots & \vdots \\ 1 & \cos \psi_i & \sin \psi_i & \cos 2\psi_i & \sin 2\psi_i & \dots & (-1)^i \\ \vdots & \vdots & \vdots & \vdots & \vdots & \vdots & \vdots \\ 1 & \cos \psi_{N_b} & \sin \psi_{N_b} & \cos 2\psi_{N_b} & \sin 2\psi_{N_b} & \dots & (-1)^{N_b} \end{pmatrix} \cdot \begin{pmatrix} q_0 \\ q_{1c} \\ q_{1s} \\ \vdots \\ q_S \end{pmatrix}. \tag{11}$$

Similar to Eq. 9, the degrees of freedom in the rotating frame can be collected in the column vector  $\mathbf{q}^R = \{q_1, \dots, q_i, \dots, q_{N_b}\}^T$  while  $\mathbf{q}^{NR} = \{q_0, q_{1c}, q_{1s}, \dots, q_S\}^T$  collects the degrees of freedom in the non-rotating frame. It should be noted that the transformation matrix reported above is time dependent,  $\mathbf{T}(t)$ , and its time derivative must be computed to correctly define the transformation between the degrees of freedom derivatives, namely:

$$\mathbf{q}^R = \mathbf{T}(t) \cdot \mathbf{q}^{NR}, \tag{12a}$$

$$\dot{\mathbf{q}}^R = \mathbf{T}(t) \cdot \dot{\mathbf{q}}^{NR} + \dot{\mathbf{T}}(t) \cdot \mathbf{q}^{NR} \tag{12b}$$

Applying the MCT to Eq. 9, the corresponding damping and stiffness matrices in the non-rotating frame are obtained, namely:

$$\mathbf{C}^{NR} = \mathbf{T}^T \mathbf{C}^R \mathbf{T}, \tag{13a}$$

$$\mathbf{K}^{NR} = \mathbf{T}^T \mathbf{K}^R \mathbf{T} + \mathbf{T}^T \mathbf{C}^R \dot{\mathbf{T}}. \tag{13b}$$

For isotropic rotors, the matrices are constants and any time dependency disappears. The non-rotating damping and stiffness matrices have the following structure:

$$\mathbf{C}^{NR} = N_b \begin{pmatrix} C_0 & & & & & & \\ & \frac{1}{2}C_1 & & & & & \\ & & \frac{1}{2}C_1 & & & & \\ & & & \frac{1}{2}C_2 & & & \\ & & & & \frac{1}{2}C_2 & & \\ & & & & & \ddots & \\ & & & & & & C_S \end{pmatrix}, \tag{14}$$



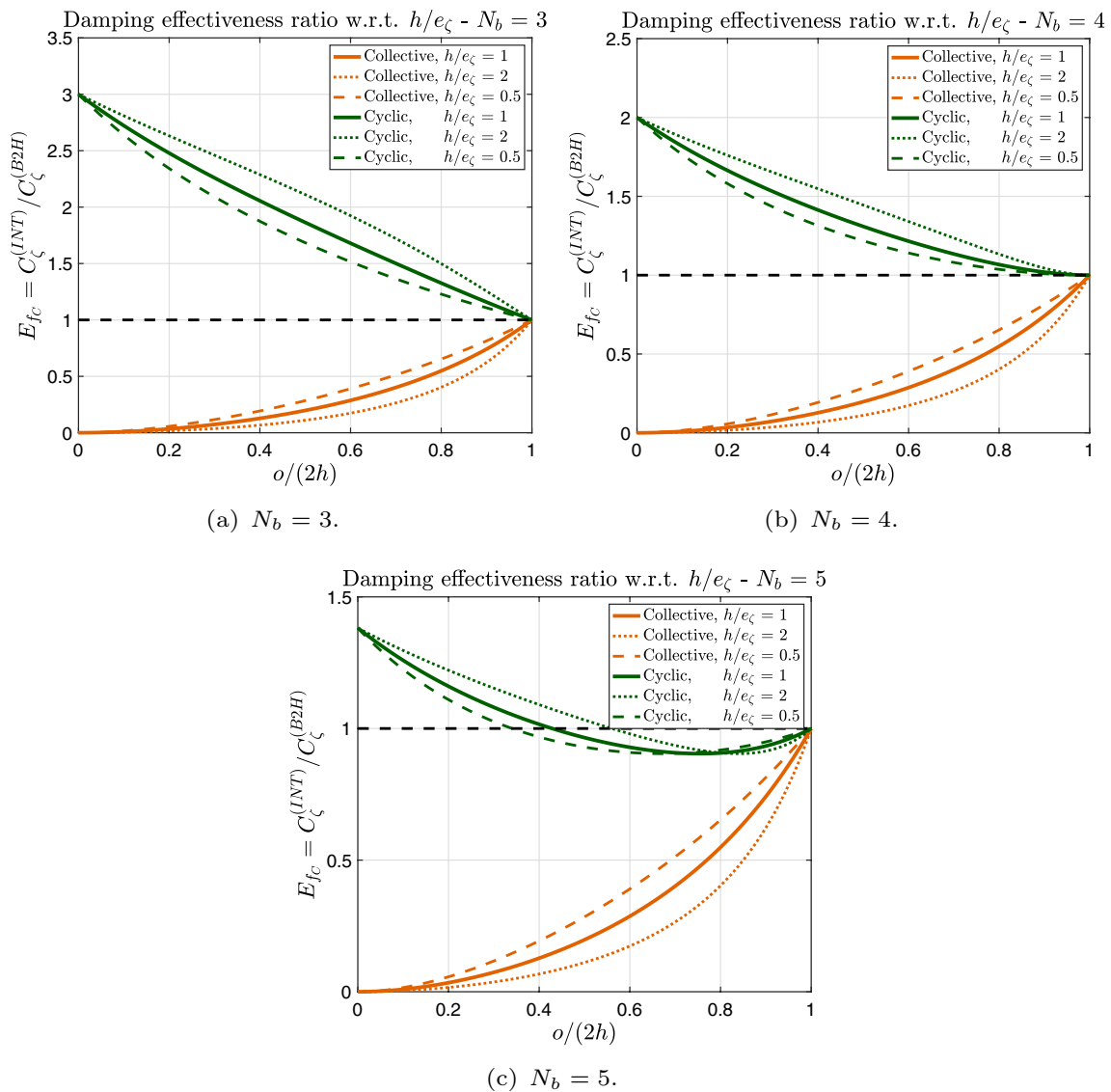


**Fig. 4** Damping effectiveness ratios  $E_{fc} = C_{\zeta}^{(INT)} / C_{\zeta}^{(B2H)}$  w.r.t. radial offset—sensitivity to the average attachment position,  $h/e_{\zeta}$

is not. The corresponding cyclic damping coefficient  $C_{\zeta}^{(B2H)}$  yields different values for  $\zeta_E \lesssim 0$ , leading to different damping effectiveness ratios.

The last sensitivity analysis is dedicated to the pre-stress effect on the stiffness effectiveness ratio (Fig. 6). Overall, the pre-stress induces an increment in the collective stiffness, even when the radial offset is null. Conversely, the cyclic stiffness shows a different behavior depending on the number of blades. For a three-bladed rotor, the pre-stress reduces the cyclic stiffness while a slight increment is observed for a five-bladed rotor. The contribution on the four-bladed rotor is instead negligible.

It should be noted that, for a five-bladed rotor, the inter-blade damper is beneficial only for limited values of the radial offset. Values of  $o/(2h)$  greater than  $\approx 0.4$  return effectiveness ratios lower than 1 for both collective and cyclic components. This limitation could be overcome by shifting the inter-blade attachment points far away from the lead-lag hinges, as shown in Fig. 4c (dotted line), considering the available space along the blade span. However, particular attention must be paid to the unfavorable kinematic couplings that might arise with the blade flap and pitch dynamics.

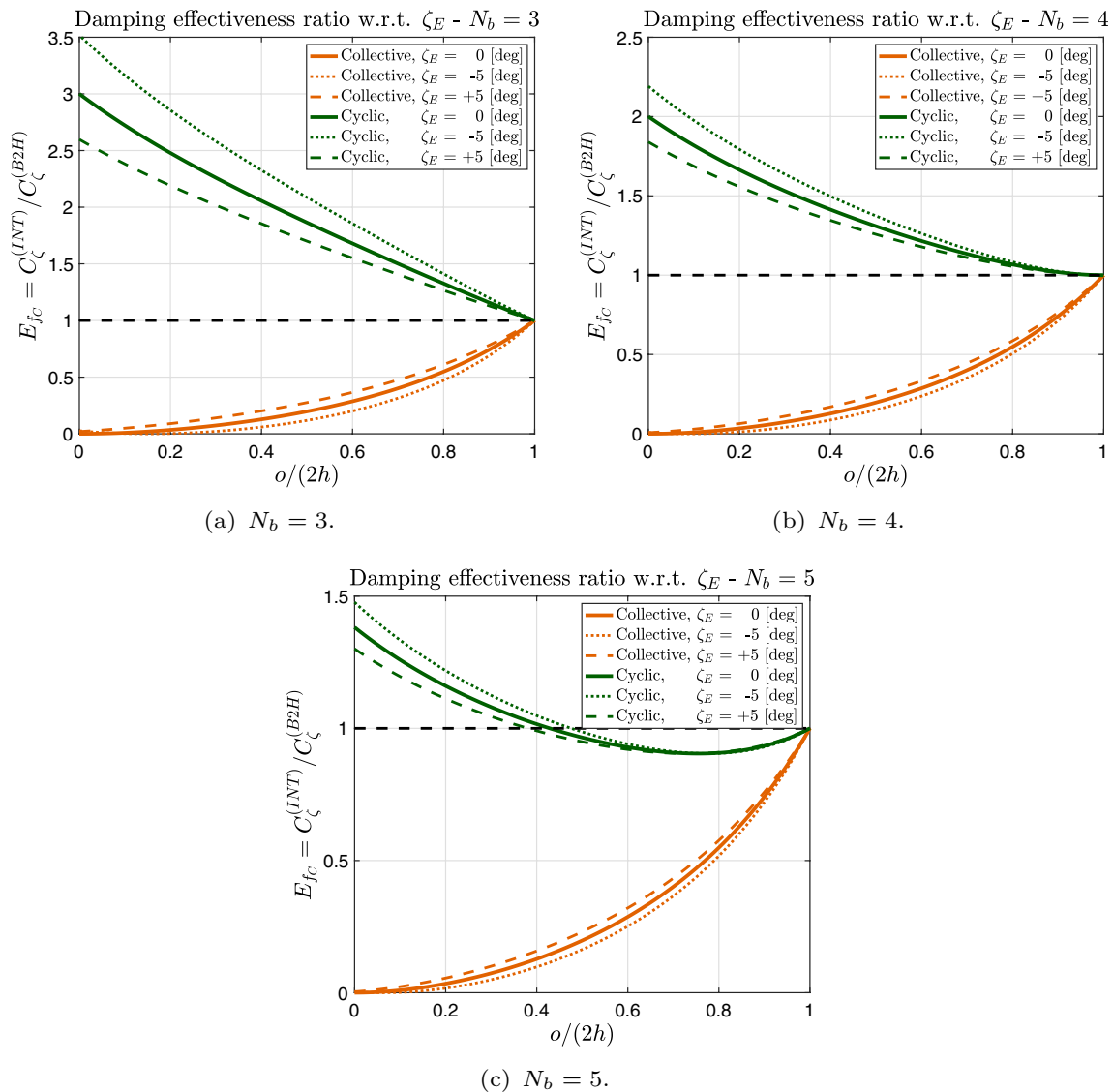


Fig. 5 Damping effectiveness ratios  $E_{fc} = C_{\zeta}^{(INT)} / C_{\zeta}^{(B2H)}$  w.r.t. radial offset—sensitivity to the lead-lag angle,  $\zeta_E$

### 3 Methodology

In the following, a more generic numerical approach is proposed to extend the inter-blade damper models to generic attachment offsets. Dampers will be included in the aeromechanical model of a four-bladed medium-size helicopter to investigate ground resonance proneness with reference to different attachment points. The helicopter model is obtained in MASST (Modern Aeroservoelastic State Space Tools, Refs. [16, 17]). The tool, developed at Politecnico di Milano, can perform different kinds of simulation, including stability and dynamic response analyses of relatively simple yet complete modular models of complex aeroservoelastic systems using general state-space approaches.

The dynamic model set-up of the helicopter for ground resonance analysis is first presented. Subsequently, the inter-blade dampers will be modeled as Linear Time Invariant (LTI) systems through linear constitutive laws and added to the helicopter model. The failure of one damper will be considered as well. This condition is specifically required for vehicle certification. Indeed, inter-blade damper models will be modified through a Linear Time Periodic (LTP) structure and ground stability analyses performed with Floquet’s approach.

#### 3.1 Dynamic model set-up

For ground resonance analysis, the characteristics of a medium-size helicopter, representative of the IAR330 Puma,



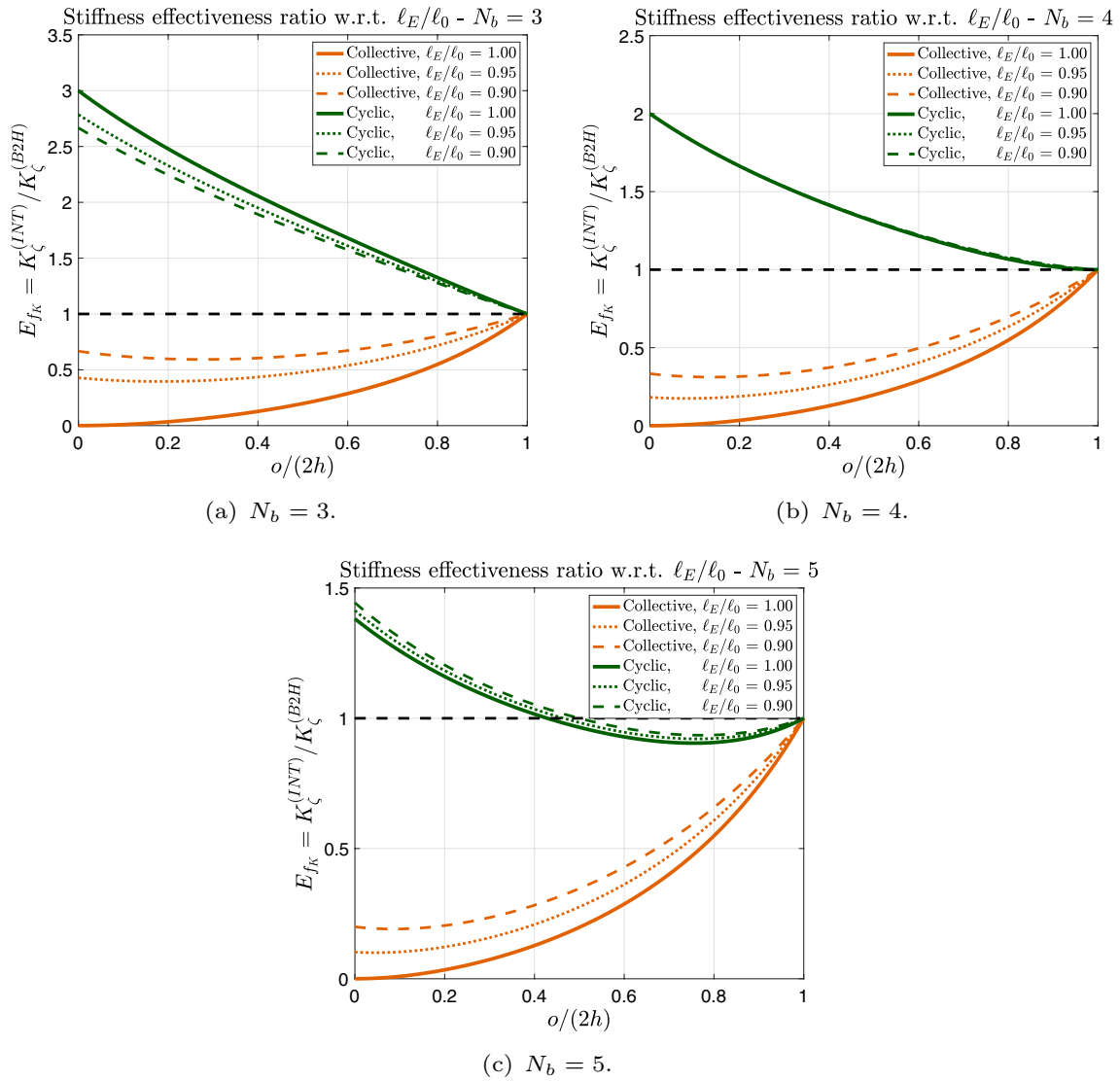


**Fig. 6** Stiffness effectiveness ratios  $E_{f_k} = K_{\zeta}^{(INT)}/K_{\zeta}^{(B2H)}$  w.r.t. radial offset—sensitivity to pre-stress,  $\ell_E/\ell_0$

**Table 2** IAR330 airframe modal parameters

Mode number	1	2	3	4	5	6
Mode name	Fore/Aft	Lateral	Plunge	Yaw	Pitch	Roll
Freq. ( $\omega_k$ ), Hz	0.345	0.376	0.989	1.332	2.376	3.169
Damp. ( $\xi_k$ ), %	0.271	0.295	0.777	1.046	1.866	2.489
Mode shape: ( $\times 10^{-2}$ )						
$T_x$ , m	1.497	-0.018	-0.401	0.011	0.150	0.006
$T_y$ , m	-0.019	-1.857	0.016	0.033	0.003	-0.629
$T_z$ , m	0.315	-0.002	1.123	0.004	0.032	-0.014
$R_x$ , rad	0.004	0.398	-0.003	-0.134	-0.003	0.548
$R_y$ , rad	0.324	-0.004	-0.072	0.003	-0.309	-0.001
$R_z$ , rad	0.000	0.010	-0.000	0.511	0.005	0.214

**Table 3** Main rotor general characteristics

Characteristic	Value	Unit
Main rotor radius	7.490	m
Main rotor solidity	0.091	n.d
Main rotor Lock number	8.700	n.d
Main rotor rotating speed	270	rpm
Main rotor flap frequency	1.030	/rev
Main rotor lag frequency	0.250	/rev

are considered. The technical data are taken from Refs. [18, 19], and from chapter 4 and the related appendix A4 of Ref. [20]. The dynamic model setup includes (1) the airframe structural model, (2) the main rotor aeroelastic model, and (3) the inter-blade damper model.

The airframe is rigid with flexible landing gears. The resulting linear model is composed of the generalized mass, damping, and stiffness matrices plus the displacements at a few noteworthy points, including the center of the main rotor hub. Table 2 lists the modal parameters of the fuselage on the ground (with unit modal mass), with the corresponding mode shapes at the main rotor hub. Mode shapes have been identified with reference to the highest modal participation. Displacements and rotations are referred to a Cartesian reference frame with the longitudinal  $x$ -axis positive from nose to tail, the lateral  $y$ -axis positive starboard, and the  $z$ -axis positive upward.

Main rotor aeroelastic models are obtained from CAM-RAD/JA using data published by Bousman et al. in Ref. [19]. Rotor dynamics are generally described by nonlinear differential equations, which can be linearized for a subset of trim configurations representative of the flight conditions of interest. Linear time-invariant models are computed using coefficient averaging to eliminate any periodicity whenever the rotors are not in axial flow conditions. A robust interpolation method is subsequently used in MASST to estimate rotor models for any intermediate trim point (Ref. [17]). For ground resonance analysis, a database of 6 linearized models has been defined for several rotor speeds, ranging from 10% to 120% of the nominal value with intermediate trim points at 25%, 50%, 75%, and 100%. The rotor has been trimmed in axial flow conditions with thrust equal to zero (100% weight on wheels) at sea-level standard ISA<sup>1</sup> + 0°C conditions. Collective, cyclic, and scissor modes have been included in the four-bladed, clockwise, articulated main rotor model, namely three bending modes, two torsion modes, along with the six hub/pylon rigid modes required to connect the rotor to the airframe. Thus, the rotor models contain 26 degrees of freedom. Specifically, the three bending modes are selected to model the rigid lead-lag and flap modes, together with

the 1st elastic beamwise mode. Similarly, the torsion modes are related to the pitch control chain compliance and the 1st elastic torsion of the blade. The rotor blade aerodynamic loads are based on lifting-line and steady two-dimensional airfoil characteristics, with corrections for unsteady and three-dimensional flow effects. The calculation of the loading at the blade tip is corrected for three-dimensional effects using a tip loss factor. Unsteady and compressible aerodynamics effects are also considered, but only the static effects of stall are taken into account. The general characteristics of the main rotor are reported in Table 3.

The main rotor aeroelastic model has been validated by comparing the blade frequencies in a vacuum and the rotor performance in hover, with analogous results obtained using the general-purpose multibody solver MBDyn. Results, presented in Ref. [21], correlate well also with those reported by Bousman et al. [19].

### 3.2 Inter-blade damper formulation

The equations for the inter-blade damper are derived from the virtual work principle (VWP), namely

$$\delta W = \sum_{i=1}^{N_b} \left( \delta \mathbf{r}_{B_{i+1}} - \delta \mathbf{r}_{A_i} \right)^T \mathbf{F}_i. \quad (17)$$

The restoring force  $\mathbf{F}_i$ , due to the  $i$ th damper, does work for the virtual relative displacement between the generic attachment points  $A_i, B_{i+1}$  of the two adjoining blades. Considering a linear visco-elastic constitutive law, the  $i$ th damper force can be written as:

$$\mathbf{F}_i = -c_i \dot{\ell}_i \hat{\mathbf{r}}_i - k_i (\ell_i - \ell_0) \hat{\mathbf{r}}_i, \quad (18)$$

including the unit vector  $\hat{\mathbf{r}}_i \triangleq \frac{\mathbf{r}_{B_{i+1}} - \mathbf{r}_{A_i}}{\|\mathbf{r}_{B_{i+1}} - \mathbf{r}_{A_i}\|}$ , with

$$\ell_i = \|\mathbf{r}_{B_{i+1}} - \mathbf{r}_{A_i}\|, \quad (19)$$

$$\dot{\ell}_i = \left( \dot{\mathbf{r}}_{B_{i+1}} - \dot{\mathbf{r}}_{A_i} \right)^T \hat{\mathbf{r}}_i. \quad (20)$$

It should be noted that even considering a linear constitutive law with reference to the damper elongation  $\ell_i$  and the corresponding rate  $\dot{\ell}_i$ , the restoring force shows a nonlinear relationship with the relative position and velocity of the attachment points. Consequently, Eq. 18 must be firstly linearized about an equilibrium condition.

In the following, the resulting linearized equations are reported as a function of the relative displacement vector  $\mathbf{r}_i \triangleq \mathbf{r}_{B_{i+1}} - \mathbf{r}_{A_i}$  and its time derivative  $\dot{\mathbf{r}}_i \triangleq \dot{\mathbf{r}}_{B_{i+1}} - \dot{\mathbf{r}}_{A_i}$ . The linearization of the  $i$ th force yields:

<sup>1</sup> International Standard Atmosphere.

$$\mathbf{F}_i \approx \mathbf{F}_i \Big|_E + \frac{\partial \mathbf{F}_i}{\partial \mathbf{r}_i^T} \Big|_E \Delta \mathbf{r}_i + \frac{\partial \mathbf{F}_i}{\partial \dot{\mathbf{r}}_i^T} \Big|_E \Delta \dot{\mathbf{r}}_i. \tag{21}$$

The derivatives in Eq. 21, evaluated at the equilibrium condition, return the  $3 \times 3$  stiffness and damping matrices reported in the following:

$$\mathbf{K}_i = - \frac{\partial \mathbf{F}_i}{\partial \mathbf{r}_i^T} \Big|_E = k_i \frac{(\ell_E - \ell_0)}{\ell_E} \mathbf{I} + k_i \frac{\ell_0}{\ell_E} \frac{\mathbf{r}_i \cdot \mathbf{r}_i^T \Big|_E}{\ell_E^2}, \tag{22}$$

$$\mathbf{C}_i = - \frac{\partial \mathbf{F}_i}{\partial \dot{\mathbf{r}}_i^T} \Big|_E = c_i \frac{\mathbf{r}_i \cdot \mathbf{r}_i^T \Big|_E}{\ell_E^2}, \tag{23}$$

where  $(\mathbf{r}_i \cdot \mathbf{r}_i^T \Big|_E) / \ell_E^2$  are direction cosine matrices, representing the attitude of the  $i$ th damper on the rotor shaft reference frame. The VWP with the linearized forces yields

$$\delta \Delta W = - \sum_{i=1}^{N_b} \delta \Delta \mathbf{r}_i^T \mathbf{C}_i \Delta \dot{\mathbf{r}}_i - \sum_{i=1}^{N_b} \delta \Delta \mathbf{r}_i^T \mathbf{K}_i \Delta \mathbf{r}_i. \tag{24}$$

The virtual work can be rewritten by collecting all variables in a global vector  $\Delta \mathbf{r}$ , so that

$$\delta \Delta W = - \delta \Delta \mathbf{r}^T \mathbf{C} \Delta \dot{\mathbf{r}} - \delta \Delta \mathbf{r}^T \mathbf{K} \Delta \mathbf{r}, \tag{25}$$

with  $\Delta \mathbf{r} = \{ \Delta \mathbf{r}_{B_1}, \Delta \mathbf{r}_{A_1}, \dots, \Delta \mathbf{r}_{B_{N_b}}, \Delta \mathbf{r}_{A_{N_b}} \}^T$ . The resulting  $6N_b \times 6N_b$  damping matrix (and similarly for the stiffness matrix) yields the following block structure:

$$\mathbf{C} = \begin{pmatrix} +\mathbf{C}_{N_b} & & & & & -\mathbf{C}_{N_b} \\ & +\mathbf{C}_1 & -\mathbf{C}_1 & & & \\ & -\mathbf{C}_1 & +\mathbf{C}_1 & & & \\ & & & \ddots & & \\ & & & & +\mathbf{C}_{N_b-1} & -\mathbf{C}_{N_b-1} \\ & & & & -\mathbf{C}_{N_b-1} & +\mathbf{C}_{N_b-1} \\ -\mathbf{C}_{N_b} & & & & & +\mathbf{C}_{N_b} \end{pmatrix}. \tag{26}$$

It should be noted that the firsts rows and columns are characterized by non-zero terms in the latest blocks, to connect the first blade with the last one through the corresponding inter-connected damper.

To restore the perturbation variables in the rotating blade reference frame an additional transformation is required, namely

$$\Delta \mathbf{r}_{B_i} = \mathbf{R}_i \Delta \mathbf{r}_{B_i}^R, \tag{27a}$$

$$\Delta \mathbf{r}_{A_i} = \mathbf{R}_i \Delta \mathbf{r}_{A_i}^R, \tag{27b}$$

where  $\Delta \mathbf{r}_{B_i}^R$  and  $\Delta \mathbf{r}_{A_i}^R$  are defined in the local  $i$ th blade reference frame and  $\mathbf{R}_i$  is the corresponding rotation matrix,

$$\mathbf{R}_i = \begin{pmatrix} +\cos(i\Delta\psi) & -\sin(i\Delta\psi) & 0 \\ +\sin(i\Delta\psi) & +\cos(i\Delta\psi) & 0 \\ 0 & 0 & 1 \end{pmatrix}. \tag{28}$$

This transformation is necessary to apply the multiblade transformation afterward, and it can be generalized through a global rotation matrix

$$\mathbb{R} = \begin{pmatrix} \mathbf{R}_1 & & & & & \\ & \mathbf{R}_1 & & & & \\ & & \mathbf{R}_2 & & & \\ & & & \mathbf{R}_2 & & \\ & & & & \ddots & \\ & & & & & \mathbf{R}_{N_b} \\ & & & & & & \mathbf{R}_{N_b} \end{pmatrix}, \tag{29}$$

so that  $\Delta \mathbf{r} = \mathbb{R} \Delta \mathbf{r}^{R(1)}$ .

Furthermore, if the two attachment points are not available in the blade discretization, the corresponding displacements can be obtained as a function of the displacements and rotations of the closest blade node  $P_i$ , considering a rigid connection, namely

$$\Delta \mathbf{r}_{B_i}^R = \Delta \mathbf{r}_{P_i}^R + \Delta \theta_{P_i}^R \times (\mathbf{r}_B - \mathbf{r}_P)^R, \tag{30a}$$

$$\Delta \mathbf{r}_{A_i}^R = \Delta \mathbf{r}_{P_i}^R + \Delta \theta_{P_i}^R \times (\mathbf{r}_A - \mathbf{r}_P)^R, \tag{30b}$$

collected in the following global matrix

$$\mathbf{Q} = \begin{pmatrix} \mathbf{I} - (\mathbf{r}_B - \mathbf{r}_P)_{\times}^R & & & & & \\ \mathbf{I} - (\mathbf{r}_A - \mathbf{r}_P)_{\times}^R & & & & & \\ & \mathbf{I} - (\mathbf{r}_B - \mathbf{r}_P)_{\times}^R & & & & \\ & \mathbf{I} - (\mathbf{r}_A - \mathbf{r}_P)_{\times}^R & & & & \\ & & \ddots & & & \\ & & & \mathbf{I} - (\mathbf{r}_B - \mathbf{r}_P)_{\times}^R & & \\ & & & \mathbf{I} - (\mathbf{r}_A - \mathbf{r}_P)_{\times}^R & & \end{pmatrix}, \tag{31}$$

where  $(\mathbf{r}_B - \mathbf{r}_P)_{\times}^R$  and  $(\mathbf{r}_A - \mathbf{r}_P)_{\times}^R$  are  $3 \times 3$  skew-symmetric matrices<sup>2</sup> defined in the local blade reference frame. The transformation is then applied through a linear operator,  $\Delta \mathbf{r}^{R(1)} = \mathbf{Q} \Delta \mathbf{r}^{R(2)}$ , with  $\Delta \mathbf{r}^{R(2)} = \{ \Delta \mathbf{r}_{P_1}^R, \Delta \theta_{P_1}^R, \dots, \Delta \mathbf{r}_{P_{N_b}}^R, \Delta \theta_{P_{N_b}}^R \}^T$ .

Each  $\Delta \mathbf{r}_{P_i}^R$  vector contains the three displacements of the blade node  $P_i$  in the local blade reference frame, namely  $\Delta \mathbf{r}_{P_i}^R = \{ \Delta x_{P_i}^R, \Delta y_{P_i}^R, \Delta z_{P_i}^R \}^T$ , and similarly for the three rota-

<sup>2</sup>  $\mathbf{a} = \{a_1, a_2, a_3\}^T$ ,  $\mathbf{a}_{\times} = \begin{pmatrix} 0 & -a_3 & a_2 \\ a_3 & 0 & -a_1 \\ -a_2 & a_1 & 0 \end{pmatrix}$ .

tions  $\Delta\theta_{P_i}^R = \left\{ \Delta\phi_{P_i}^R, \Delta\vartheta_{P_i}^R, \Delta\psi_{P_i}^R \right\}^T$ . Before applying the MCT the  $\Delta\mathbf{r}^{R(2)}$  vector is reordered to collect all the longitudinal, lateral and vertical displacements followed by the corresponding rotations, through a permutation matrix  $\Delta\mathbf{r}^{R(2)} = \mathbb{P}\Delta\mathbf{r}^{R(3)}$ , with

$$\Delta\mathbf{r}^{R(3)} = \left\{ \begin{matrix} \Delta\mathbf{r}_P \\ \Delta\theta_P \end{matrix} \right\}^R = \left\{ \begin{matrix} \Delta\mathbf{x}_P \\ \Delta\mathbf{y}_P \\ \Delta\mathbf{z}_P \\ \Delta\phi_P \\ \Delta\vartheta_P \\ \Delta\psi_P \end{matrix} \right\}^R = \left\{ \begin{matrix} \Delta x_{P_1} \\ \Delta x_{P_2} \\ \vdots \\ \Delta x_{P_{N_b}} \\ \Delta y_P \\ \Delta z_P \\ \Delta\phi_P \\ \Delta\vartheta_P \\ \Delta\psi_P \end{matrix} \right\}^R. \quad (32)$$

Finally, the MCT is applied through a  $(6N_b \times 6N_b)$  block diagonal matrix  $\mathbb{T}(t)$ , containing the  $\mathbf{T}(t)$  matrices defined in Eq. 11 on the diagonal blocks, such that  $\Delta\mathbf{r}^{R(3)} = \mathbb{T}(t)\Delta\mathbf{r}^{NR}$ , and  $\dot{\Delta\mathbf{r}}^{R(3)} = \dot{\mathbb{T}}(t)\Delta\mathbf{r}^{NR} + \mathbb{T}(t)\dot{\Delta\mathbf{r}}^{NR}$ .

The global damping and stiffness matrices, in the non-rotating frame, are finally obtained through the VWP,

$$\mathbb{C}^{NR} = \mathbb{T}^T \mathbb{P}^T \mathbb{Q}^T \mathbb{R}^T \mathbb{C} \mathbb{R} \mathbb{Q} \mathbb{P} \mathbb{T}, \quad (33a)$$

$$\mathbb{K}^{NR} = \mathbb{T}^T \mathbb{P}^T \mathbb{Q}^T \mathbb{R}^T (\mathbb{K} \mathbb{R} \mathbb{Q} \mathbb{P} \mathbb{T} + \mathbb{C} \mathbb{R} \mathbb{Q} \mathbb{P} \dot{\mathbb{T}}). \quad (33b)$$

The matrices are constants for isotropic rotors with  $c_d = c_1, \dots, c_{N_b}$  and  $k_d = k_1, \dots, k_{N_b}$ . The proposed approach can manage dissimilar dampers as well, leading to time periodic stiffness and damping matrices. The corresponding modal matrices can be easily obtained through the rotor mode shapes, in multiblade coordinates, applied to Eq. 33. Once obtained, the inter-blade modal damping and stiffness matrices can be added to the rotor aeroelastic matrices.

### 4 Ground resonance stability analysis

Stability analyses in MASST are performed using a continuation procedure (Ref. [22]), making it possible to follow the evolution of only the desired subset of eigensolutions of the system for the different parameter values. The Coleman diagrams reported in the following display the real ( $\sigma$ ) and imaginary ( $\omega$ ) parts of the eigenvalues with reference to the rotor speed. The system is stable if the real part of all eigenvalues is negative. The fuselage pitch and roll eigenmodes, together with the lead-lag collective and cyclic roots (progressive and regressive), have been followed by the continuation procedure for RPM values ranging from 10% to 120%

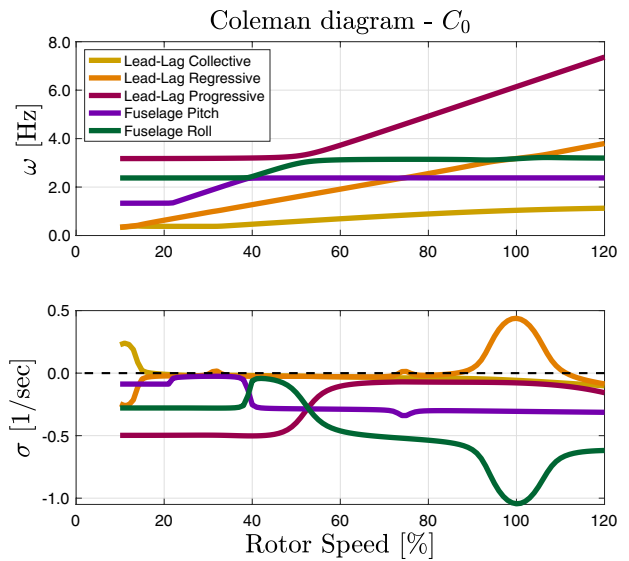


Fig. 7 Coleman diagrams for the evolution of the helicopter model eigenvalues with RPM; configuration  $C_0$  without lead-lag dampers

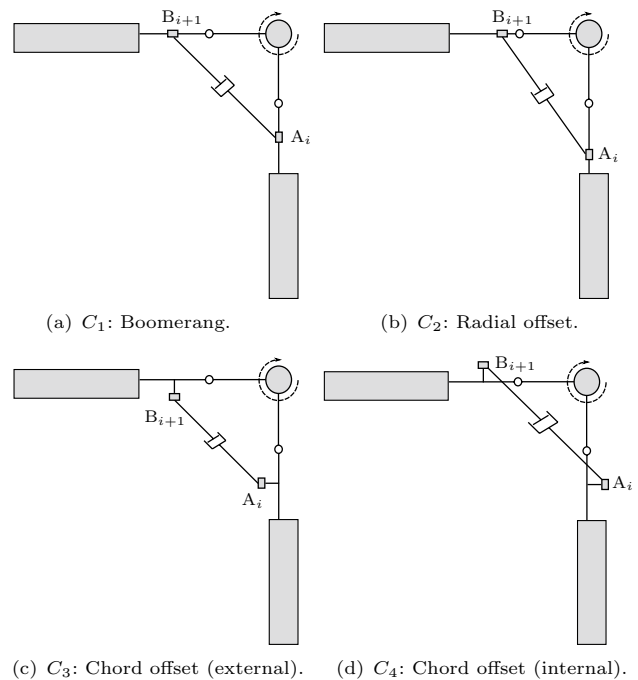


Fig. 8 Inter-blade configurations with in-plane offsets

of the nominal value. It must be remarked that the mode shapes of the coupled rotor-fuselage system are hybridized. The mode assignment in the Coleman diagrams has been carried out with reference to the highest modal participation evaluated at 120% of the rotor speed. Results, without lead-lag dampers, are shown in Fig. 7.

This configuration is referred to as  $C_0$ . The typical instability “bubbles” appear on the real part of the eigenvalues;

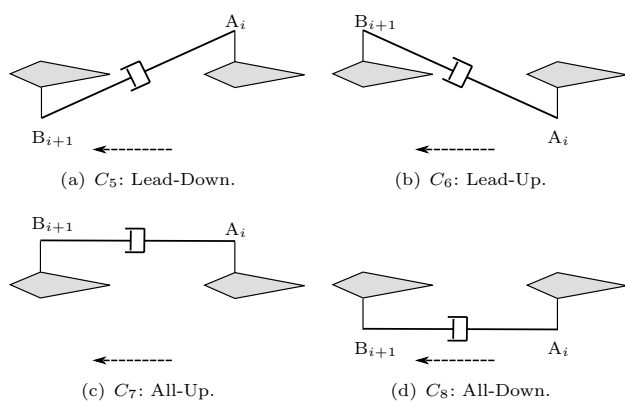


Fig. 9 Inter-blade configurations with out-of-plane offsets

the critical condition is obtained at the nominal RPM, due to the coalescence of the lead-lag cyclic regressive mode with the fuselage roll mode.

In the following, the inter-blade dampers are included in the helicopter model. Stability analyses are performed for different attachment offsets in radial, chordwise and vertical directions to investigate the effects of each configuration on ground resonance.

### 4.1 Inter-blade configurations

Eight different configurations, depicted in Figs. 8 and 9, have been investigated in this work starting from the classical boomerang configuration without offsets, referred to as  $C_1$ . The next configuration,  $C_2$ , includes a radial offset, while both the  $C_3$  and  $C_4$  configurations provide respectively an external and internal chordwise offset. Please, note that the IAR330 Puma main rotor rotates in the clockwise direction, with the advanced blade depicted on the left in Fig. 8. It must be stressed that the results presented in the following do not change for a counterclockwise rotor.

The four configurations shown in Fig. 9 include out-of-plane offsets. Configuration  $C_5$  (Damper Lead-Down) is characterized by a negative vertical offset at the “leading edge” of the damper, while the “trailing edge” is given a positive offset. For the configuration,  $C_6$  (Damper Lead-Up) offsets are reversed. Configuration  $C_7$  (All-Up) shows positive vertical offsets for all inter-blade dampers, while for configuration  $C_8$  (All-Down) offsets are negative.

The articulated IAR330 Puma main rotor includes the lead-lag hinge at 3.59% of the radial span, followed by the flap hinge at 3.86%, and the pitch bearing at 5.77%. For the baseline boomerang configuration, the inter-blade attachment points are located at 8% of the radial span, outboard of the 3 hinges. Radial, in-plane, and out-of-plane offsets have been introduced with an offset of 1%  $r/R$  from the baseline attachment point.

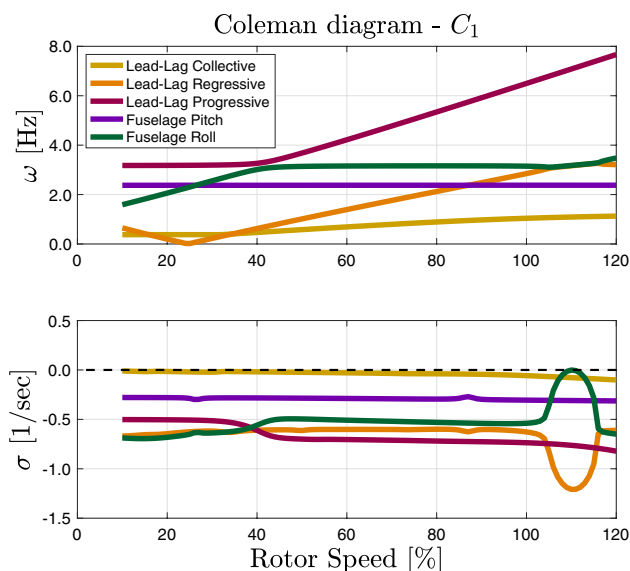


Fig. 10 Coleman diagrams for the evolution of the helicopter model eigenvalues with RPM; configuration  $C_1$ —baseline boomerang inter-blade dampers

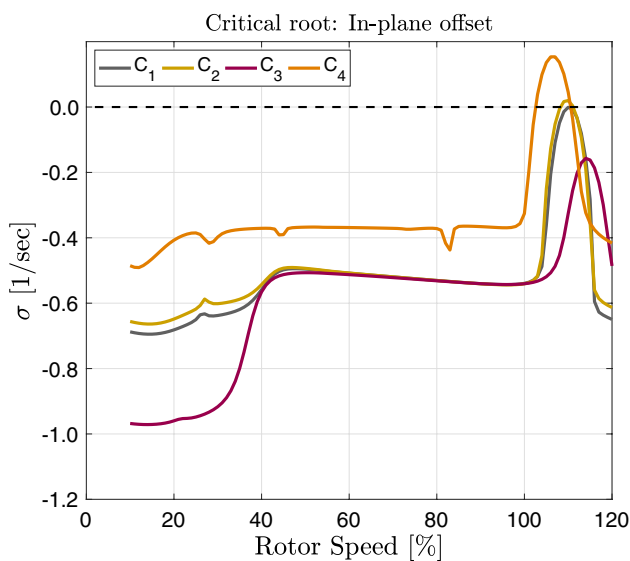
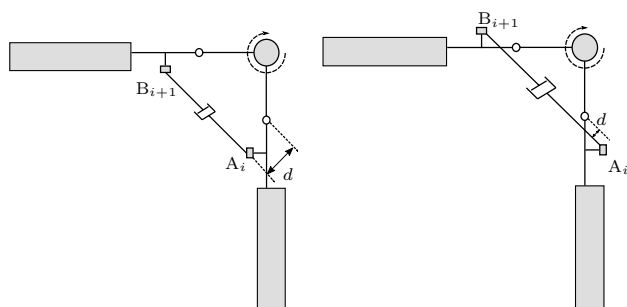


Fig. 11 Evolution of the critical root (real part) with RPM for different in-plane offsets on inter-blade dampers

### 4.2 Discussion of results

For the work presented here, an elastic coefficient of  $k_d = 500$  N/mm has been selected, representative of a quasi-linear elastomeric damper model for a helicopter of the same category. The viscous coefficient has been specifically selected to obtain limit stability conditions for the baseline boomerang configuration, namely  $c_d = 12.9$  N·s/mm. Figure 10 depicts the Coleman diagrams for the IAR330 Puma helicopter with boomerang dampers. The stiffness



(a)  $C_3$ : Chord offset (external). (b)  $C_4$ : Chord offset (internal).

**Fig. 12** Inter-blade configurations with chord offsets—equivalent arm

contribution on inter-blade dampers slightly modifies the cyclic (and the scissor) lead-lag frequencies. The resonance with the fuselage roll mode is now shifted at 110% RPM. The ground resonance bubble is contained inside the stability region (negative real part). The critical root reaches the zero damping condition with a resonance frequency of 3.18 Hz. The lead-lag collective root is not modified since the only source of damping is related to the in-plane generalized aerodynamic forces.

The introduction of a small in-plane offset modifies helicopter stability. The evolution of the critical root for the first four configurations is shown in Fig. 11. The radial offset (configuration  $C_2$ ) increases the lead-lag collective damping at the expense of the cyclic component, leading to a mild ground resonance instability. A positive (external) chord offset leads to a stabilizing effect (configuration  $C_3$ ), increasing both the lead-lag stiffness and damping cyclic components, thanks to the higher arm between the inter-blade attachment points and the lead-lag hinges, as shown in Fig. 12a. The opposite trend is obtained with a negative (internal) chord offset (configuration  $C_4$ ), characterized by a reduced arm (Fig. 12b), and leading to a ground resonance phenomenon.<sup>3</sup> Configuration  $C_3$  could be a good solution to reduce ground resonance proneness, maintaining the same damper characteristics. However, this configuration requires specific care for the design of the attachment parts, since high local stresses on the corner edges could be present due to the additional in-plane bending moments provided by the dampers.

The evolution of the critical root when considering out-of-plane offsets on inter-blade dampers is depicted in Fig. 13. Stability analyses show that configurations  $C_5$  (Lead-Down) and  $C_7$  (All-Up) both improve ground resonance stability margins. Conversely, configurations  $C_6$  (Lead-Up) and  $C_8$  (All-Down) destabilize the helicopter on the ground.

### 4.3 The role of main rotor pitch dynamics

The different ground resonance behaviors when changing out-of-plane offsets of inter-blade dampers is due to the main

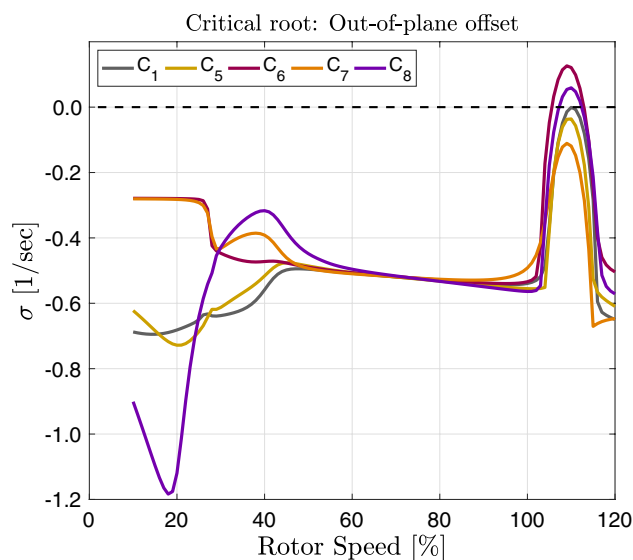


**Fig. 13** Evolution of the critical root (real part) with RPM for different out-of-plane offsets on inter-blade dampers

rotor pitch dynamics, whose main contribution is due to the control chain compliance. Pitch dynamics are characterized by faster transients when compared to the first lead-lag and flap dynamics. Specifically, the collective pitch frequency on the IAR330 Puma main rotor is found at 5.6/rev. Despite the large frequency separation, it is the quasi-static response of pitch dynamics that plays a fundamental role in ground resonance when vertical offsets on inter-blade dampers are considered, by changing the reference configuration of the main rotor blades and, consequently, the cyclic lead-lag viscous damping,  $C_\zeta$ , and the pitch-lag coupling,  $K_{p\zeta}$ . The last is a kinematic feedback of lag displacement to the blade pitch motion, namely:  $\Delta\theta = -K_{p\zeta} \cdot \zeta$ . For positive values of  $K_{p\zeta}$  (lag-back, pitch-down), the resulting contribution acts as a restoring moment on the blade dynamics, leading to a stabilizing effect [23]. The pitch-lag coupling can be achieved in many ways, including skewed lag hinges or with a specific design of the pitch control linkages. It also depends on the blade reference configuration and elastic deformation. In this work, the  $K_{p\zeta}$  coefficient is computed from the stiffness matrix of the rotor, after quasi-static approximation of the pitch and elastic torsion modes, together with the 1st elastic beamwise mode.<sup>4</sup> The reduced model obtained is only

<sup>3</sup> Indeed, it is easy to relate the lead-lag damping (and stiffness) cyclic coefficient for a rigid rotor through the arm  $d$ , namely  $C_\zeta = 2c_d d^2$ .

<sup>4</sup> The quasi-static approximation is obtained by dropping the acceleration and velocity terms due to the high-frequency modes, preserving their static contribution. The obtained reduced-order models retain the low-frequency dynamics, together with the static effect of the high-frequency modes [24, 25].

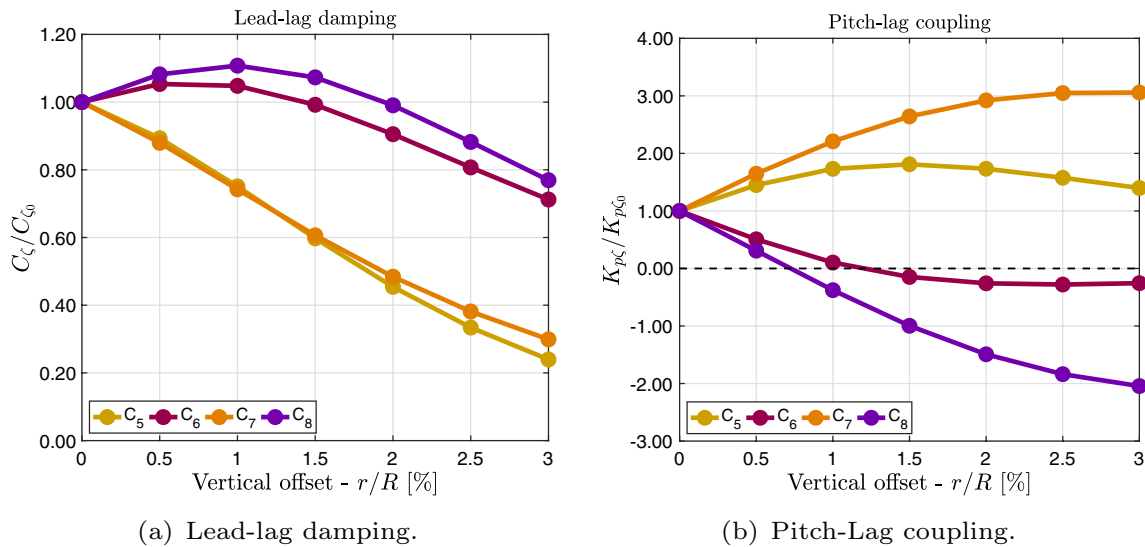


Fig. 14 Evolution of cyclic lead-lag damping (left) and pitch-lag coupling (right) w.r.t. vertical offset at RPM = 110%

characterized by the rigid flap-lag degrees of freedom. The linearized flap-lag equations of motion are well-known in the literature (see, for example, chapter 20 of Ref. [24]). Hence, the rotor parameters can be easily identified from the matrices of the reduced system. Specifically, the pitch-lag coupling is extracted from the generalized flap force, whose dimensionless contribution due to the lag is  $M_\zeta = \gamma/8 \cdot K_{p\zeta}$ , where  $\gamma$  is the Lock number. Indeed, the kinematic coupling is captured when considering the rotor aerodynamic loads, usually not included in classical ground resonance analysis.

It should be pointed out that the quasi-static response of the elastic torsion mode has a smaller impact on the pitch-lag coupling, since the main effect relies on the control chain compliance which modifies the pitch measured on the pitch bearing when compared to the imposed pitch driven by the pilot’s controls. The contribution due to the 1st elastic beam-wise mode is instead negligible.

Figure 14 compares the cyclic lead-lag damping and the pitch-lag coupling obtained with the four inter-blade configurations proposed in Fig. 9 with reference to a variable vertical offset. All curves are obtained for a rotor speed of 110%, where the coalescence between the fuselage roll mode and lead-lag regressive mode is found. The reference cyclic lead-lag damping coefficient  $C_{L0}$  and pitch-lag coupling  $K_{pL0}$  are referred to the boomerang configuration.

Figure 14a displays a lead-lag damping reduction for both the Lead-Down (C<sub>5</sub>) and All-Up (C<sub>7</sub>) configurations with reference to the vertical offset, while for the Lead-Up (C<sub>6</sub>) and All-Down (C<sub>8</sub>) configurations an increment is initially observed, followed by a damping reduction for higher vertical offset values.

Nevertheless, the largest stability margins on GR obtained for the Lead-Down (C<sub>5</sub>) and All-Up (C<sub>7</sub>)

configurations are due to the pitch-lag couplings shown in Fig. 14b. The two configurations C<sub>5</sub> and C<sub>7</sub> are both characterized by higher pitch-lag couplings when compared to the boomerang configuration. The effective lag mode damping is increased by positive pitch-lag coupling coefficients, which highlights how this kinematic coupling can improve ground/air resonance characteristics, as suggested by Bousman [23, 26] and verified by Zotto and Loewy [27].

However, it should be noted that the behavior does not display a monotonic trend. Indeed, the maximum value for the C<sub>5</sub> configuration is obtained for a vertical offset equal to  $r/R = 1.5\%$ , while a slope reduction is noticed for the C<sub>7</sub>

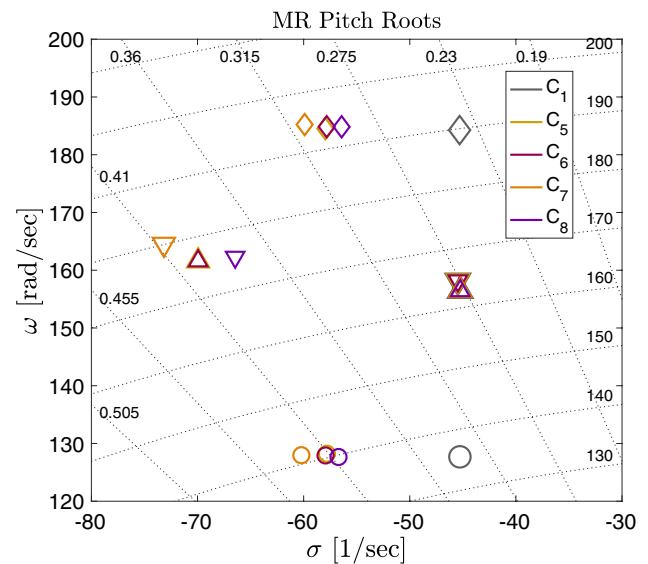


Fig. 15 Main rotor pitch roots for different vertical offsets on inter-blade dampers. Reg. (○), Coll. (△), Sc. (▽), Prog. (◇)

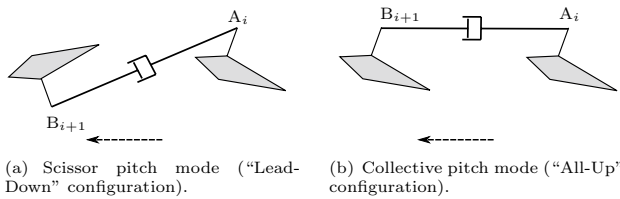


Fig. 16 Rigid mechanism on inter-blade dampers with vertical offsets

(All-Up) configuration, leading to a pitch-lag coupling reduction for larger vertical offsets. The Lead-Up and All-Down configurations, respectively  $C_6$  and  $C_8$ , are instead characterized by the opposite trend, leading to negative (unstable) pitch-lag couplings, with an adverse impact on GR stability.

Overall, the Lead-Down and All-Up configurations should be favored to improve the helicopter’s stability on the ground. The selection of the optimal vertical offset would require a trade-off study since an increment on the pitch-lag coupling is usually balanced with a corresponding reduction in the lead-lag damping. For the Lead-Down configuration, the trade-off study could be restricted to vertical offsets up to  $r/R = 1.5\%$ , since higher values lead to a reduction in both the pitch-lag coupling and lead-lag damping.

Finally, it should be noted that a vertical offset on inter-blade dampers provides additional damping on the main rotor pitch dynamics. Collective, cyclic and scissor pitch roots are shown in Fig. 15 for the baseline boomerang configuration, compared with analogous results obtained with the inter-blade dampers characterized by vertical offsets.

The main rotor pitch dynamics are often poorly damped. All inter-blade configurations with vertical offsets increase

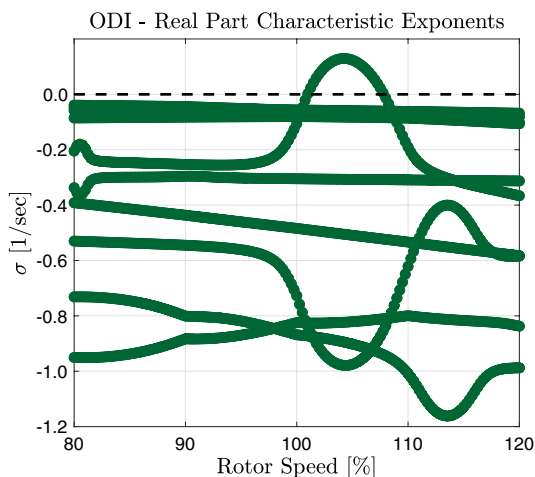
the damping ratio of the cyclic regressive and progressive pitch roots. The configurations Lead-Up and Lead-Down ( $C_5$  and  $C_6$ ) increase the collective pitch damping as well. The scissor component remains unaltered. Conversely, the two configurations All-Up and All-Down ( $C_7$  and  $C_8$ ) do not modify the original collective pitch damping, while the scissor pitch root moves to the left part of the Argand Plane. The different behavior is easily explained by the rigid mechanism shown in Fig. 16. The scissor pitch mode, for the Lead-Up and Lead-Down configurations, does not supply a damper deformation. A similar mechanism is obtained with the collective pitch mode for the All-Up and All-Down configurations.

Vertical offsets on inter-blade dampers can be specifically designed to avoid ground resonance phenomena, as well as with an improvement on the main rotor pitch stability.

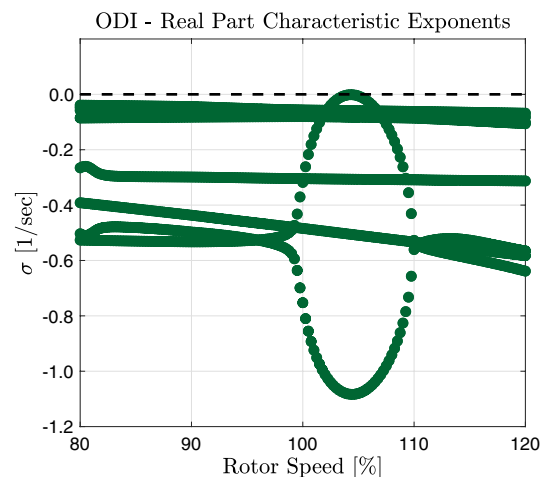
### 4.4 One damper inoperative

The last section investigates GR proneness with one damper inoperative (ODI). This condition is required for rotorcraft certification (see subsection 663(a) of Refs. [28, 29]).

The global damping and stiffness matrices related to the inter-connected dampers are still obtained from Eq. 33, now characterized by periodic coefficients with  $T = 2\pi/\Omega$ . The periodic state matrix  $\mathbb{A}$  is obtained representing the inter-connected dampers as a control system connected in feedback to the helicopter dynamics. The starting point is a linear model of the helicopter that takes as input the restoring forces due to the inter-connected dampers and provides as output the dampers’ elongation and the relative



(a)  $c_d = 12.9 \text{ N}\cdot\text{s} / \text{mm} - k_d = 500 \text{ N} / \text{mm}$ .



(b)  $c_d = 27.1 \text{ N}\cdot\text{s} / \text{mm} - k_d = 500 \text{ N} / \text{mm}$ .

Fig. 17 GR analysis with inter-blade boomerang dampers. Real part of the Floquet’s characteristic exponents for One Damper Inoperative (ODI) condition



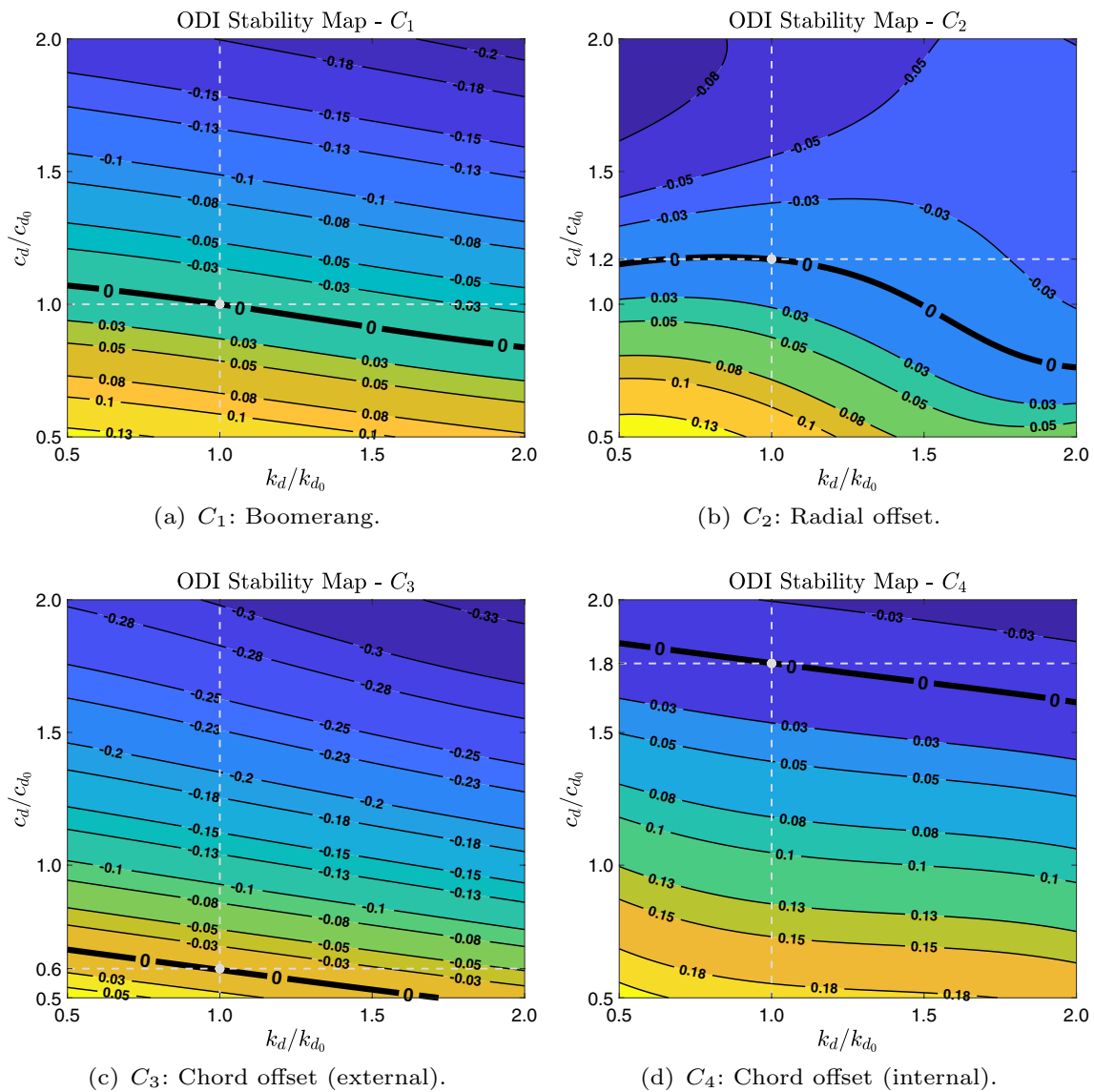


Fig. 18 One Damper Inoperative stability maps. Inter-blade configurations with in-plane offsets

velocity, represented through the helicopter state-space matrices  $\mathbf{A}_H, \mathbf{B}_H, \mathbf{C}_H$  obtained from MASST. Then the dampers are described through a time-periodic gain matrix  $\mathbf{G}(t) = (\mathbb{K}^{NR}, \mathbb{C}^{NR})$  leading to the periodic state matrix

$$\mathbf{A}(t) = \mathbf{A}_H - \mathbf{B}_H \mathbf{G}(t) \mathbf{C}_H. \tag{34}$$

Stability analyses of the closed-loop LTP systems are performed using the Floquet theory [30].

Floquet characteristic exponents have been initially evaluated for the boomerang configuration ( $C_1$ ) with one damper inoperative, maintaining the reference values for the viscous damping and stiffness coefficients, namely  $c_d = 12.9 \text{ N}\cdot\text{s}/\text{mm}$  and  $k_d = 500 \text{ N}/\text{mm}$ . The real part of the characteristic exponents is shown in Fig. 17a with reference to the rotor

speed ranging from 80% to 120% of the nominal value. A GR instability is detected between 101% and 108% of the nominal rotor speed.

To restore a stable system, with one damper inoperative, it is necessary to increase the viscous coefficient up to the value of  $27.1 \text{ N}\cdot\text{s}/\text{mm}$ , i.e. more than twice its original value, as depicted in Fig. 17b. In the following, this value will be used as a reference for GR stability analyses performed with ODI, i.e.  $c_{d_0} = 27.1 \text{ N}\cdot\text{s}/\text{mm}$ . The reference value of the stiffness coefficient is not modified, i.e.  $k_{d_0} = 500 \text{ N}/\text{mm}$ .

Sensitivity analyses of the viscous and stiffness coefficients have been performed through the stability maps shown in Fig. 18 when considering inter-blade configurations with in-plane offsets, and in Fig. 19 for out-of-plane offsets. The two parameters range between  $0.5\times$  and  $2.0\times$

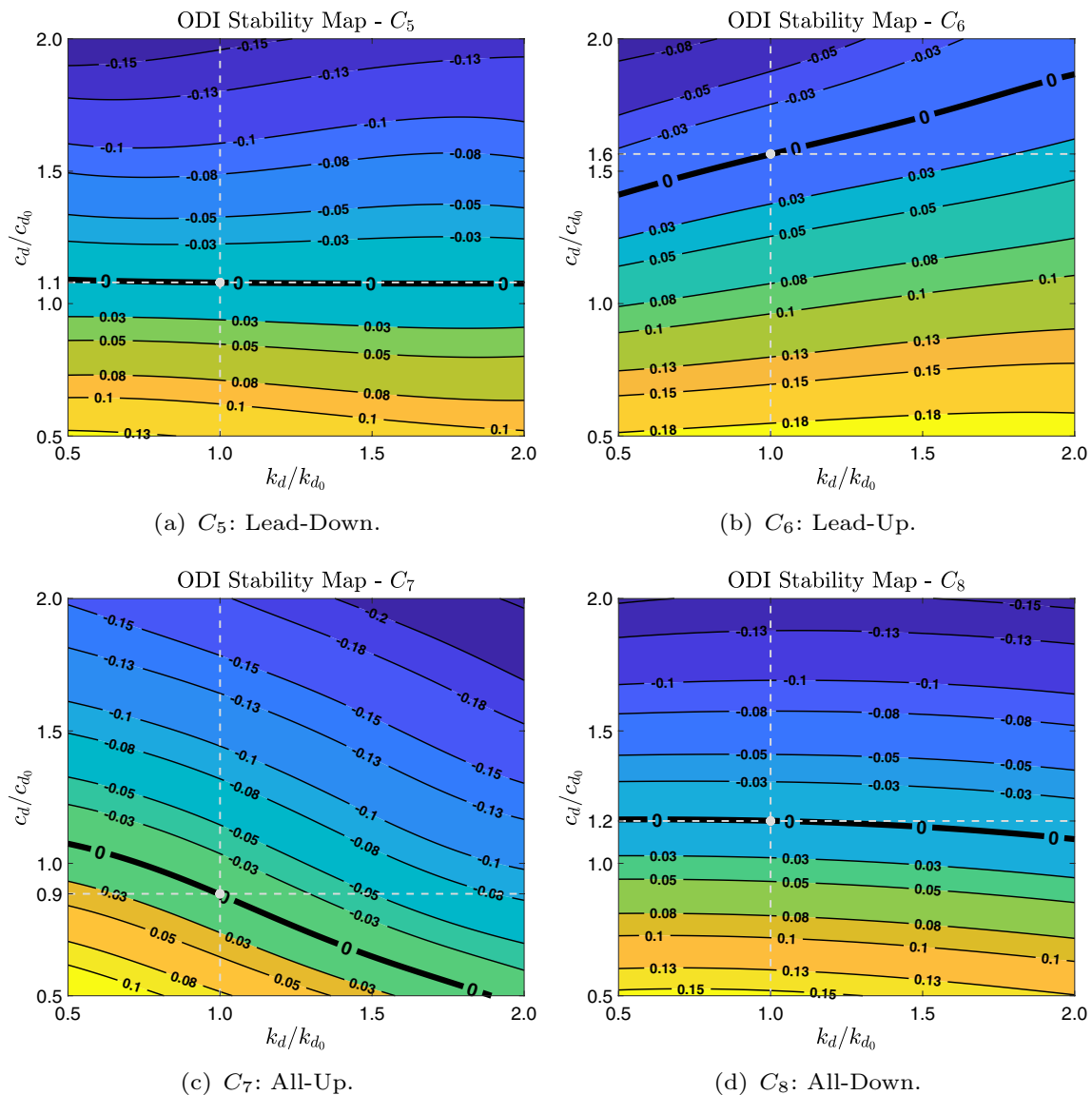


**Fig. 19** One Damper Inoperative stability maps. Inter-blade configurations with out-of-plane offsets

their nominal values. Stability maps show the peak value of the real part of the critical Floquet's characteristic exponent, obtained for RPM ranging between 80% and 120% of the nominal rotor speed. The stability boundaries are remarked with a thicker black line for each configuration. Again, negative values of the real part of the critical characteristic exponents are referred to a stable system.

The boomerang configuration ( $C_1$ , Fig. 18a) clearly shows that an increment in the stiffness coefficient reduces the amount of viscous damping necessary to maintain a stable condition. Indeed, for GR stability a high lag frequency is desired [2].

The introduction of a radial offset requires, as expected, more damping to stabilize the rotorcraft on the ground, as depicted in Fig. 18b. Once again, increasing  $k_d$ , the stability

boundaries are reached for smaller viscous coefficients. This configuration requires particular attention since two resonance conditions are detected for specific values of  $c_d$  and  $k_d$ . The nature of the second instability is discussed at the end of this section and requires the reader a brief reminder of periodic systems stability. Indeed, the stability maps here presented have been generated considering the most critical characteristic exponent, namely the one with the real part closest to zero for a stable system or, conversely, the one with the largest positive real part.

An external chord offset shows the positive effects in the stability map of Fig. 18c, even for ODI conditions. A reduced viscous damping (60% of the nominal value) is sufficient to stabilize the LTP system, maintaining the nominal stiffness coefficient. Conversely, an internal chord offset

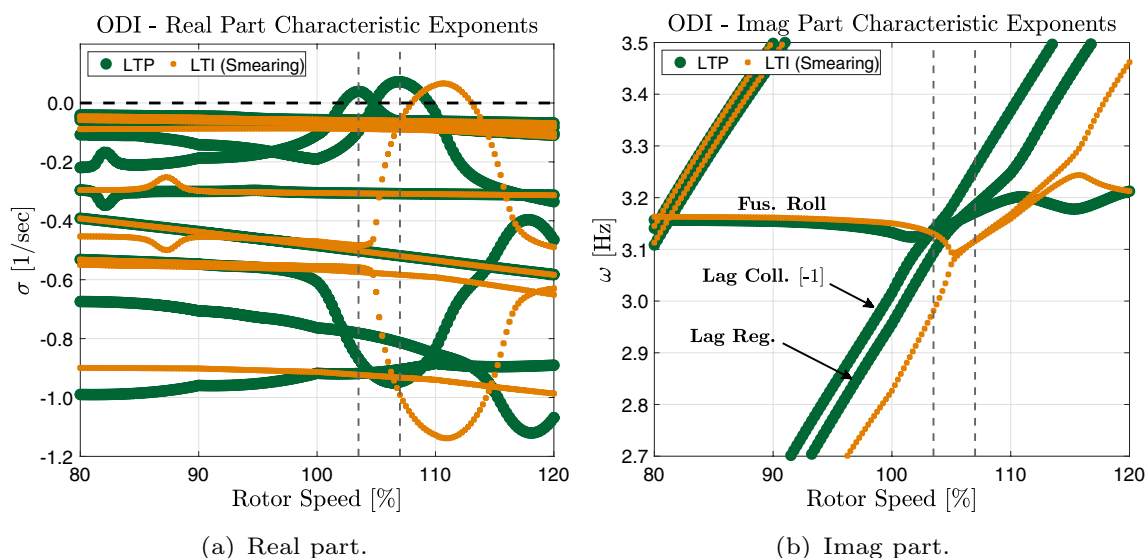


**Fig. 20** Inter-blade damper with radial offset ( $C_2$ ) and One Damper Inoperative,  $c_d/c_{d_0} = 0.5$ ,  $k_d/k_{d_0} = 1.5$ . Floquet’s analysis on LTP system vs eigenanalysis on LTI system obtained with smearing technique

requires a strong increment on  $c_d$  to restore a stable solution, as depicted in Fig 18d. Increasing the stiffness coefficient slightly helps the system to improve the stability boundaries for the last two analyzed conditions.

Stability maps for out-of-plane offsets are discussed in the following. The Lead-Down configuration is first investigated (Fig. 19a). A slight increment in the viscous coefficient is required to obtain a stable system. Moreover, this configuration seems poorly affected by the stiffness coefficient, whose gradient results almost null for the range of values taken into account.

The Lead-Up configuration requires a significant increment in the viscous coefficient to reach the stability boundaries. Moreover, increasing the stiffness term leads to worse stability conditions, due to the reverse gradient shown in Fig. 19b. Indeed, the stiffness coefficient and the pitch-lag coupling are characterized by an opposite trend for this configuration.

Figure 19c depicts the stability map for the All-Up configuration. A considerable improvement is obtained by increasing the stiffness coefficient leading, for this case, to larger pitch-lag couplings. The positive effect on GR is also confirmed for ODI conditions.

The last configuration, All-Down—Fig. 19d, requires a 20% increment on the inter-blade damper viscous coefficient to restore a stable system, while the stiffness term has a negligible impact.

The periodic stability analysis for ODI conditions almost confirms the trend observed on isotropic rotors when different inter-blade damper configurations are taken into account. Additionally, the Floquet analysis clearly shows how a significant increment of damping (more than twice the nominal

value used for the isotropic rotor), is required to restore a stable system.

The section ends with the analysis of the dual instability observed with the inter-blade dampers with radial offset (configuration  $C_2$ ). The real part of the Floquet characteristic exponents is shown, for this configuration, in Fig. 20a with  $c_d/c_{d_0} = 0.5$  and  $k_d/k_{d_0} = 1.5$ . To identify the mode shapes involved in GR instability, the imaginary part of the Floquet characteristic exponents is computed as well, which return the frequencies, showing all possible resonances, including parametric ones (see Fig. 20b). It must be remembered that, for each Floquet characteristic exponent,  $\eta_j$ , computed by the corresponding characteristic multiplier,<sup>5</sup>  $\Lambda_j$ , the periodic stability analysis reveals the presence of a fan made by an infinite number of harmonics, or super-harmonics, of varying strength, namely:

$$\eta_j = \frac{1}{T} \ln \|\Lambda_j\| + i \cdot \frac{1}{T} \arctan \frac{\Im(\Lambda_j)}{\Re(\Lambda_j)} + i \cdot n \frac{2\pi}{T} \quad (35)$$

where  $n$  is an arbitrary integer between  $\pm\infty$ . Several methodologies are proposed in the literature to determine the strength of all the integer-multiple components, or to select the dominant frequency [31–33]. In this work, for each Floquet characteristic multiplier, a finite number of super-harmonics has been computed and classified (from the most to the less dominant), using the approach proposed by Lopez and Prasad in Ref. [34]. The method is based on the

<sup>5</sup> The characteristic multipliers are the eigenvalues of the monodromy matrix [30].

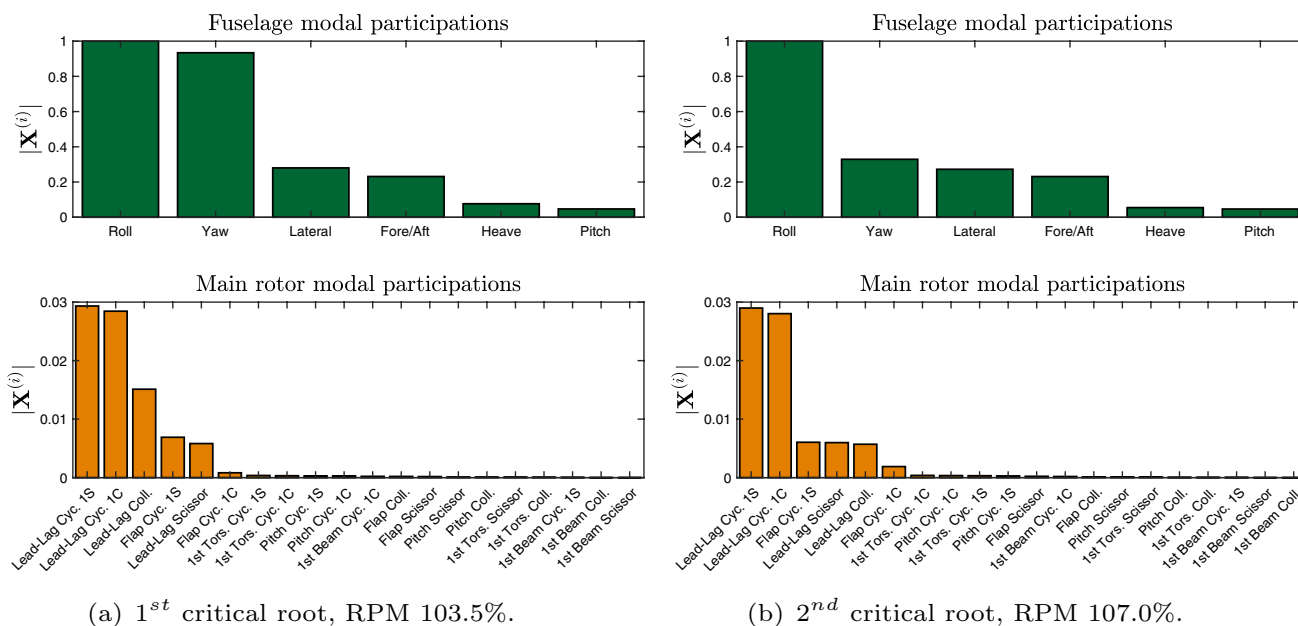


**Fig. 21** Inter-blade damper with radial offset ( $C_2$ ) and One Damper Inoperative,  $c_d/c_{d_0} = 0.5$ ,  $k_d/k_{d_0} = 1.5$ . Modal participations of the two critical roots

evaluation of the complex-exponential harmonic coefficients of the periodic eigenvector.

Two resonance conditions can be detected in Fig. 20b. The first at 103.5% and the second at 107% of the nominal rotor speed. The corresponding eigenvectors related to the critical, unstable, roots are depicted in Fig. 21, normalized to obtain maximum participation equal to 1. The first critical root, whose modal participation is shown in Fig. 21a, is characterized by a huge participation of both the fuselage roll and yaw modes, while the lead-lag cyclic and collective modes are mainly involved for the main rotor. It is found that the ODI condition hybridizes the lead-lag collective and cyclic modes. Indeed, the resonance at 103.5% is due to a super-harmonic of the lead-lag collective mode at  $-\frac{2\pi}{T}$ , referred to as with the label “Lag. Coll. [− 1]” in Fig. 20b, now combined with the lead-lag cyclic dynamics. Please, note that the instability is not predicted by the corresponding LTI system obtained with the smearing technique since the eigenanalysis does not provide any super-harmonic. These results prove that, for the ODI condition with inter-blade dampers and radial offsets:

- the lead-lag collective and cyclic modes are hybridized;
- the lead-lag super-harmonics may interact with the airframe/fuselage roots, generating additional resonances;
- stability analyses must be performed with the Floquet theory, considering the system periodicity, avoiding any equivalent, approximated LTI system.

Finally, the second critical root at 107% shows a similar behavior to the classical GR for articulated rotors, due to the coalescence of the lead-lag regressive mode with the fuselage roll mode, as depicted by the modal participations in Fig. 21b.

### 5 Conclusions

Linearized models of inter-blade dampers connected to aeroelastic rotors through generic blade attachment points are presented and used for ground resonance analysis of a medium-size helicopter.

Initially, an analytical approach is exploited to obtain a simple formulation for the lead-lag damping and stiffness parameters of inter-blade dampers with radial offsets only. The approach is suitable for sensitivity analyses of the main parameters. The effectiveness ratio, which compares the inter-blade collective and cyclic components with those of the classical blade-to-hub configuration, is evaluated and discussed. The results clearly show how the radial offset decreases the inter-blade performance on the cyclic components, increasing the lead-lag collective damping and stiffness terms. Moreover, for a five-bladed rotor, the inter-blade configuration is found to be beneficial only for limited values of radial offsets. The analytical formulation can be used to define the optimal location of the inter-blade attachment points to avoid ground resonance phenomena and to

stabilize the engine drive-train dynamics through the addition of damping on the lead-lag collective dynamics, when high gains on the fuel control system are present.

Subsequently, a more generalized approach for inter-blade damper models with generic in-plane and out-of-plane attachment offsets is proposed. Inter-blade dampers are modeled as linear time invariant and linear time-periodic systems. Ground resonance stability analyses are performed on a four-bladed, medium-size, helicopter representative of the IAR330 Puma, considering inter-blade dampers with different offsets. Eight inter-blade configurations have been investigated, starting from the classical boomerang one without offsets. The first configurations include radial and chordwise offsets. The last four consist of out-of-plane offsets. A visco-elastic constitutive law is considered. The baseline boomerang configuration returns a resonance at 110% of the nominal rotor speed between the lead-lag regressive mode and the fuselage roll mode. The radial offset increases the lead-lag collective damping at the expense of the cyclic component, leading to a mild instability. A positive (external) chord offset leads to a stabilizing effect thanks to the higher arm between the inter-blade attachment points and the lead-lag hinges. However, it should be remarked that this configuration produces higher local stress on the attachment points. The opposite trend is obtained with the internal chord offset.

Different results are obtained when considering vertical offsets on inter-blade dampers, due to the quasi-static response of the main rotor pitch dynamics on lead-lag and flap dynamics. Specifically, it is demonstrated that the inter-blade configurations leading to an increment on the pitch-lag coupling ( $K_{p\zeta}$ , positive for lag back, pitch down) improve the helicopter stability margins. However, the selection of the optimal vertical offset requires a trade-off study since an increment on the pitch-lag coupling is usually balanced with a corresponding reduction on the lead-lag damping. These effects are captured when considering the overall blade motions, including flap, lag, and pitch dynamics, together with the corresponding generalized aerodynamics forces, usually neglected on classical ground resonance analysis. Among all configurations tested, the one with all positive vertical offsets (designated “All-Up”) returns a significant improvement in ground resonance stability.

Finally, ground resonance analyses are performed with one damper inoperative, using the Floquet theory for linear time periodic systems. To restore a stable condition it is necessary to double the damper viscous coefficient. Sensitivity analyses of the damper viscous and stiffness coefficients are performed through stability maps. The periodic stability analysis almost confirms the trend observed for isotropic rotors. Particular attention should be given to the inter-blade configuration with radial offsets that, in the case of one damper inoperative, may return multiple resonance

conditions. The paper shows how, for this specific condition, the lead-lag collective and cyclic modes are hybridized, and how the corresponding super-harmonics, due to the system periodicity, may lead to unstable roots.

**Funding** Open Access funding enabled and organized by CAUL and its Member Institutions.

**Open Access** This article is licensed under a Creative Commons Attribution 4.0 International License, which permits use, sharing, adaptation, distribution and reproduction in any medium or format, as long as you give appropriate credit to the original author(s) and the source, provide a link to the Creative Commons licence, and indicate if changes were made. The images or other third party material in this article are included in the article's Creative Commons licence, unless indicated otherwise in a credit line to the material. If material is not included in the article's Creative Commons licence and your intended use is not permitted by statutory regulation or exceeds the permitted use, you will need to obtain permission directly from the copyright holder. To view a copy of this licence, visit <http://creativecommons.org/licenses/by/4.0/>.

## References

1. Coleman, R.P.: Theory of self-excited mechanical oscillations of hinged rotor blades. ARR 3G29, NACA (1943)
2. Deutsch, M.L.: Ground vibrations of helicopters. *J. Aeronaut. Sci.* **13**(5), 223–234 (1946). <https://doi.org/10.2514/8.11359>
3. Coleman, R.P., Feingold, A.M.: Theory of self-excited mechanical oscillations of helicopter rotors with hinged blades. Report 1351, NACA (1958)
4. Donham, R.E., Cardinale, S.V., Sachs, I.B.: Ground and air resonance characteristics of a soft in-plane rigid-rotor system. *J. Am. Helicopter Soc.* **14**(4), 33–41 (1969). <https://doi.org/10.4050/JAHS.14.33>
5. Ormiston, R.A.: Rotor-fuselage dynamics of helicopter air and ground resonance. *J. Am. Helicopter Soc.* **36**(2), 3–20 (1991). <https://doi.org/10.4050/JAHS.36.2.3>
6. Sela, N.M., Rosen, A.: Ground resonance of a helicopter with inter-connected blades. *J. Am. Helicopter Soc.* **36**(2), 82–85 (1991). <https://doi.org/10.4050/JAHS.36.82>
7. Sela, N.M., Rosen, A.: The influence of alternate inter-blade connections on ground resonance. *J. Am. Helicopter Soc.* **39**(3), 75–78 (1994). <https://doi.org/10.4050/JAHS.39.75>
8. Sela, N.M., Rosen, A.: Modeling the influence of inter-blade connections and variable rotor speed on the aeromechanical stability of a helicopter. *Aerosp. Sci. Technol.* **4**(3), 173–188 (2000). [https://doi.org/10.1016/S1270-9638\(00\)00125-5](https://doi.org/10.1016/S1270-9638(00)00125-5)
9. Masarati, P., Frison, L., Zanoni, A.: The inter-2-blade lead-lag damper concept. In: Proceedings of the 78th Vertical Flight Society Annual Forum, Fort Worth, pp. 1–8 (2022)
10. Kryszynski, T., Ferullo, D.: Overview of the EC155 dynamics validation program from design state up to certification. In: Proceedings of the 55th Annual Forum of the American Helicopter Society, pp. 1079–1086 (1999)
11. Suresh, J.K., Nagabhushanam, J.: Response, loads and stability of rotors with interconnected blades. *J. Am. Helicopter Soc.* **41**(4), 283–290 (1996). <https://doi.org/10.4050/JAHS.41.283>
12. Suresh, J.K., Nagabhushanam, J.: Response, loads, and stability of interconnected rotor-body systems. *J. Aircr.* **34**(3), 416–426 (1997). <https://doi.org/10.2514/2.2186>

13. Brackbill, C.R., Smith, E.C., Lesieutre, G.A.: Aeromechanical stability and response of helicopters with interblade elastomeric dampers. In: American Helicopter Society Aeromechanics Specialists Meeting, Atlanta (2000)
14. Gelb, A., Velde, W.E.V.: Multiple-Input Describing Functions and Nonlinear System Design. McGraw Hill Book Company, New York (1968)
15. Muscarello, V., Quaranta, G.: Multiple input describing function for non-linear analysis of ground and air resonance. In: 37th European Rotorcraft Forum, Gallarate. Paper no. 111 (2011)
16. Masarati, P., Muscarello, V., Quaranta, G.: Linearized aeroservoelastic analysis of rotary-wing aircraft. In: 36th European Rotorcraft Forum, Paris, pp. 099–110 (2010)
17. Masarati, P., Muscarello, V., Quaranta, G., Locatelli, A., Mangone, D., Riviello, L., Viganò, L.: An integrated environment for helicopter aeroservoelastic analysis: the ground resonance case. In: 37th European Rotorcraft Forum, Gallarate, pp. 177–112 (2011)
18. Dieterich, O., Götz, J., Dang Vu, B., Haverdings, H., Masarati, P., Pavel, M.D., Jump, M., Gennaretti, M.: Adverse rotorcraft-pilot coupling: Recent research activities in Europe. In: 34th European Rotorcraft Forum, Liverpool (2008)
19. Bousman, W.G., Young, C., Toulmay, F., Gilbert, N.E., Strawn, R.C., Miller, J.V., Maier, T.H., Costes, M., Beaumier, P.: A comparison of lifting-line and CFD methods with flight test data from a research Puma helicopter. TM 110421, NASA (1996)
20. Padfield, G.D.: Helicopter Flight Dynamics: The Theory and Application of Flying Qualities and Simulation Modeling. AIAA Ed. Series (2007)
21. Muscarello, V., Masarati, P., Quaranta, G.: Robust aeroservoelastic analysis for the investigation of rotorcraft pilot couplings. In: 3rd CEAS Air & Space Conference, Venice (2011)
22. Cardani, C., Mantegazza, P.: Continuation and direct solution of the flutter equation. *Comput. Struct.* **8**(2), 185–192 (1976). [https://doi.org/10.1016/0045-7949\(78\)90021-4](https://doi.org/10.1016/0045-7949(78)90021-4)
23. Bousman, W.G.: The effects of structural flap-lag and pitch-lag coupling on soft inplane hingeless rotor stability in hover. Technical Paper 3002, NASA (1990)
24. Johnson, W.: Rotorcraft Aeromechanics. Cambridge University Press, Cambridge (2013)
25. Johnson, W.: CAMRAD/JA, A Comprehensive Analytical Model of Rotorcraft Aerodynamics and Dynamics. Johnson Aeronautics (1988)
26. Bousman, W.J.: An experimental investigation of the effects of aeroelastic couplings on aeromechanical stability of a hingeless rotor helicopter. *J. Am. Helicopter Soc.* **26**(1), 46–54 (1981). <https://doi.org/10.4050/JAHS.26.1.46>
27. Zotto, M.D., Loewy, R.G.: Influence of pitch-lag coupling on damping requirements to stabilize “ground/air resonance”. *J. Am. Helicopter Soc.* **37**(4), 68–71 (1992). <https://doi.org/10.4050/JAHS.37.68>
28. European Aviation Safety Agency: Certification specifications, acceptable means of compliance and guidance material for small rotorcraft, amendment 8. Certification Specifications CS-27, EASA, Cologne (2021)
29. European Aviation Safety Agency: Certification specifications, acceptable means of compliance and guidance material for large rotorcraft, amendment 9. Certification Specifications CS-29, EASA, Cologne (2021)
30. Floquet, G.: Sur les équations différentielles linéaires à coefficients périodiques. *Annales scientifiques de l'École Normale Supérieure Série 2 Tome 12*, 47–88 (1883)<https://doi.org/10.24033/asens.220>
31. Borri, M.: Helicopter rotor dynamics by finite element time approximation. *Comput. Math. Appl.* **12**(1 PART A), 149–160 (1986). [https://doi.org/10.1016/0898-1221\(86\)90092-1](https://doi.org/10.1016/0898-1221(86)90092-1)
32. Nagabhushanam, J., Gaonkar, G.H.: Automatic identification of modal damping from floquet analysis. *J. Am. Helicopter Soc.* **40**(2), 39–42 (1995). <https://doi.org/10.4050/jahs.40.39>
33. Saberi, H., Xin, H., Khoshlahjeh, M.: An enhanced method for floquet modal identification. In: American Helicopter Society Specialists Conference on Aerodynamics, San Francisco, pp. 109–118 (2008)
34. Lopez, M.J.S., Prasad, J.V.R.: Technical note: Estimation of modal participation factors of linear time periodic systems using linear time invariant approximations. *J. Am. Helicopter Soc.* (2016). <https://doi.org/10.4050/JAHS.61.045001>

**Publisher's Note** Springer Nature remains neutral with regard to jurisdictional claims in published maps and institutional affiliations.